TECHNISCHE UNIVERSITÄT WIEN

DIPLOMARBEIT

Evaluation of Magnesiothermic Reduction of Ordered Mesoporous SiO_2 to Mesoporous Silicon for Si-anode Materials

Ausgeführt am Institut für

Anorganische Chemie – Funktionelle Materialien
der Universität Wien

unter der Anleitung von Prof. Dr. Freddy Kleitz und Dr. Rémy Guillet-Nicolas
als verantwortlichen mitwirkenden Universitätsassistenten

durch

Lukas Sallfeldner BSc

Datum

Unterschrift (Student)

Table of Contents

Acknowledgments

The completion of this project could not have been possible without the help of my supervisor Dr. Rémy Guillet-Nicolas who was helping me with scientific and practical advice from his new workplace in France. I would also like to thank Prof. Freddy Kleitz and all the members of his group for always offering me their help, if it was needed.

A debt of gratitude is also owed to Dr. Alexander Beutl from the Austrian Institute of Technology, who worked with us on this project. I also would like to thank Dr. Seung Won Han from the Korean Advanced Institute of Science and Technology for taking over measurements that weren't possible to execute for us, due to the pandemic situation.

Finally, I want to thank my family, in particular my parents Mr. and Mrs. Sallfeldner and my grandparents Mr. and Mrs. Piber. Without their support over the last years none of this would indeed be possible.

Abstract

Renewable energy sources (RES) are slowly replacing unsustainable sources such as gasoline and coal, to lead us to a more environmentally sound future. The problem RES are facing is that the energy generation is highly weather-dependent, and therefore inconsistent. Energy storage systems are necessary to guarantee an efficient distribution of energy when it's needed. Battery systems, especially Li-Ion-Batteries (LIBs), are the storage devices of choice currently, due to their outstanding specific and volumetric capacities combined with solid cycle stability and high energy densities. Nevertheless, the demand for LIBs with higher energy densities and capacities is growing from year to year, urging research to look for alternative materials. Silicon has an outstanding theoretical capacity depending on the Li_xSi_y phase, (i.e., 3579 or 4200 $mAh.g^{-1}$), which is about ten times higher than graphite (372 $mAh.g^{-1}$). The downside of silicon is that forming an alloy with Li leads to a substantial, irreversible specific and volumetric capacity loss, due to volume expansion (280-400 %) and solid electrolyte interface (SEI) formation during charge/discharge process.

In this master's thesis project, studies on different protocols to synthesize mesoporous Si anode materials with enhanced cycle stability and specific charge values were conducted. Ordered mesoporous silicas (OMS) with different pore structures and particle sizes were used as starting materials for magnesiothermic reduction to silicon anode materials. Mesoporous silicon with high porosity and specific surface areas of 280 $m^2.g^{-1}$ (K1 made from KIT-6) were obtained. Unfortunately, heat accumulation appeared to be a serious problem, melting the ordered pore structures and original particle shape. Nevertheless, the average pore size of samples remained in the range of the starting materials (4-22 nm). An adapted reduction protocol including the use of NaCl as a heat modulator didn't decrease thermal effects and pore closing during reduction. The electrochemical performance of the materials is better than that of purchasable nanoparticles with 130 nm, for 70-80 cycles. Especially, Si/C electrodes prepared with MCM-48-type MSNs have increased specific charge values (580 $mAh.g^{-1}$). Furthermore, studies of samples analysed after different etching post-treatments showed that hazardous HF-treatment is not necessary to obtain phase pure silicon with physio-chemical properties equivalent to samples etched with HF, if the ratio of the starting materials is correct.

Abbreviations and Acronyms

AIT	Austrian Institute of Technology
ALC	Active Lithium Content
BET	Brunauer-Emmett-Teller
BEVs	(Full) Battery Electric Vehicles
CA	Conducting Agent
CCCV	Constant Current Constant Voltage
CMC	(Sodium) Carboxy Methylcellulose
CV	Constant Voltage
CVD	Chemical Vapor Deposition
DMC	Dimethyl Ethylene Carbonate
EC	Ethylene Carbonate
EMC	Ethyl-Methyl Carbonate
EVs	Electric Vehicles
FEC	Fluoroethylene Carbonate
FFG	Austrian Research Promotion Agency
HEVs	Hybrid Electric Vehicles
HPEVs	Hybrid Plug-In Vehicles
LIB	Lithium-Ion-Battery
mSi	Mesoporous Silicon
MSNs	Mesoporous Silica Nanospheres
MTMO	Mesoporous Transition Metal Oxid
Ni-MH	Nickel-Metal Hydride
NLDFT	Non-Local Density Functional Theory
OMS	Ordered Mesoporous Silica
PAA	Poly(Acrylic Acid)
RES	Renewable Energy Sources
SEI	Solid Electrolyte Interface
SEM	Scanning Electron Microscope
SSA	Specific Surface Area
TEA	Triethylamine
(HR-)TEM	(High Resolution-) Transmission Electron Microscope
TEOS	Tetraethyl Orthosilicate
VC	Vinylene Carbonate
XRD	X-Ray Diffraction

1 Introduction

1.1 Renewable Energy Storage

In order to reduce the effects of climate change originating from the current unsustainable use of fossil fuels, new generations of safer and greener electrical energy storage systems are needed. Enhanced storage possibilities would support the integration of the growing renewable energy generation into the existing energy system by increasing the productivity of Renewable Energy Sources (RES).[1] RES include all energy sources which are continually replenished through nature. RES also have the advantage of emitting less greenhouse gases into our planet's atmosphere during energy generation. Furthermore, every country in the world has access to RES. The common sources of renewable energy are biomass and hydropower, as well as wind, solar, and geothermal energy. The big problem that remains for energy from all RES is its incapability to be stored and sent efficiently when needed. Also, the generation of renewable energy often depends on the weather conditions.[2] Different types of energy storage are already in use, including chemical, electrochemical, mechanical, electrical, and thermal techniques. Batteries, hydrogen, and flywheel storage are some of the most prominent examples for accumulation of energy from RES. While each method has aspects speaking for its use, in general batteries are by far the most used medium for electrochemical storage around the world.[3] Besides the storage of energy from RES, other application areas, for example stationary and portable electronics for consumer electronics would also profit from better energy storage options.[4] Even of higher interest is the rapidly growing market of electric vehicles (EVs), including full battery electric vehicles (BEVs), hybrid electric vehicles (HEVs) and hybrid plug-in electric vehicles (HPEVs).[5] All these sectors relying on RES share the same goal for the future, to finally become competitive to unsustainable alternatives like gasoline, in terms of performance and price.[6]

1.2 Lithium-Ion Batteries

Currently, supercapacitors and batteries are considered to be the most effective electrochemical energy storage and conversion devices for any application that requires short charging times and high performances.[7] In the sector of energy storage and conversion, Li-ion batteries (LIBs) are expected to dominate the market for at least the next ten years because of their outstanding specific and volumetric electrode capacities[8] [9], combined with solid cycle stability and high

energy densities.[10] Eq. 1 and 2 shows how to calculate the theoretical specific and volumetric capacities of an electrode material. In the equations n is the count of charge carriers (for Li = 1), F is the Faraday constant (96485.3 C/mol), and $Mw_{electrode}$ and $\rho_{electrode}$ are the molecular weight and the density of the electrode material.

$$Q_{specific} = \frac{n * F}{3600 * Mw_{electrode}}\ mAh.g^{-1} \quad \text{(eq.1)}$$

$$Q_{volumetric} = \quad Q_{specific} * \rho_{electrode}\ mAh.cm^{-3} \quad \text{(eq.2)}$$

Li-ion-batteries benefit from Li being the third lightest element with a very small ionic radius. The low weight also results in Li being the element with the highest charge-to-weight ratio, a crucial factor especially for electromobility applications. The small size of Li also positively influences diffusion processes during charging/discharging. Ionic diffusion into the solid electrolytes is often the rate-limiting factor for battery power performance. Even though the single charged Li-ions may have a lower charge capacity per ion, compared to multivalent cations, their mobility outperforms other systems.[11] In comparison to LIBs, other battery types including cobalt, manganese, nickel, or phosphorous (e.g., Ni-MH batteries) have worse properties for the typical applications areas of batteries.[12] [13]

Besides portable electronics, EVs, or smart grids, there are many other applications where LIBs play a fundamental role to make our life more comfortable and straightforward. In comparison with the alternatives, taking their energy from non-sustainable sources, this happens in a more environmentally sound way. Together with the application areas, also the demand on LIBs steadily increased in the last years. Soon, covering the growing number of annually needed batteries could become a problem, which is why new batteries with enhanced performance are necessary. Unfortunately, researchers are slowly facing the problem of reaching batteries theoretical performance limit. In 2021, the growth rate of energy density for LIBs has decreased from 7 % to 2 % per year, although next-generation high performance LIBs are highly in demand around the world.[14] [15]

The problem with currently available LIBs is the limited performance of their electrode materials. At present, graphitic carbon is the state-of-the-art material for the negative electrode (anode) of LIBs.[16] [17] [18] However, graphite experiences capacity fading at high charge and discharge rates. Furthermore, the material has a relatively low theoretical charge capacity of 372 $mAh.g^{-1}$, which is due to lithium storage via formation of LiC_6 (eq.3). [19]

$$Li + 6\ C \rightarrow LiC_6 \quad \text{(eq.3)}$$

There are two ways for improvement: the use of high-voltage cathode materials or of high-capacity electrode materials. Achieving better battery performance by increasing the cells voltage with high-voltage cathodes is problematic since state-of-the-art organic electrolytes (e.g., $LiPF_6$ in a mixture of ethylene carbonate (EC) – dimethyl carbonate (DMC)) experience decomposition if a cell attains a voltage of 4.2 V against Li/Li^+. Cathodes, usually lithium metal oxides ($LiMO_2$; e.g., $LiCoO_2$) already work at the edge of electrolyte decomposition. Additives can slightly improve the performance of the electrolyte, but until next generation high voltage resistant electrolytes are commercialized, the more promising route to enhance LIBs' performance is to increase the maximum available capacity of electrode materials.[20] [21]

1.3 Silicon as an Anode Material

Many materials have been proposed to replace graphite as the anode material for LIBs. Some of the most prominent studies include carbon nanotubes (1100 mAh.g-1) [22], graphene (960 $mAh.g^{-1}$) [23], SiO (1600 $mAh.g^{-1}$) [24], germanium (1600 $mAh.g^{-1}$) [25], tin (994 $mAh.g^{-1}$) [26], and transition metal oxides (500-1000 $mAh.g^{-1}$). [27] [28] [29]

Of all the potential new anode materials, silicon (Si) is seen as one of the most promising for the next-generation of high energy Li-ion batteries.[30] Their most outstanding property is the very high theoretical specific capacity, which is about ten times higher than graphite. In theory, capacities of 3579 or 4200 $mAh.g^{-1}$ can be achieved with silicon as anode material.[31] [32] *In situ* TEM images of a nanobattery during lithiation gave more insights into the reaction mechanism of the two Li_xSi_y phases emerging. The formation of $Li_{15}Si_4$ at room temperature and on amorphous $Li_{22}Si_5$, formed at higher temperatures was confirmed (eq.4, 5).[33]

$$15\ Li + 4\ Si \rightarrow Li_{15}Si_4 \quad (Q_{theoretical} = 3579\ mAh.g^{-1}) \qquad \text{(eq.4)}$$

$$22\ Li + 5\ Si \rightarrow Li_{22}Si_5 \quad (Q_{theoretical} = 4200\ mAh.g^{-1}) \qquad \text{(eq.5)}$$

Si also has a low electrochemical potential compared to Li/Li^+ (between 0.37 and 0.45 V) which is beneficial for anode active materials.[34] [35] [36] It is also the second most abundant element on earth and is relatively inexpensive. The impact of the extraction of crude materials for Li_xSi_y electrodes on the environment is also smaller than that of crude oil extraction. A further key advantage of Si is its high theoretical volumetric capacity (8303 $mAh.cm^{-3}$), an increasingly important feature for battery miniaturization in recent electronics.

Silicon has several characteristics which make it more suitable than graphite for the next generation of high-performance LIB's anode materials. However, there are two major problems preventing its commercialization. The first main shortcoming of Si anodes is the dramatic volume changes (280-400 %) that occur during lithium alloying/dealloying which lead to progressive pulverization and electric contact loss, causing irreversible capacity losses during the first charge-discharge cycles (fig. 1a, b). [37] [38] Secondly, there are significant, long-term irreversible capacity losses due to continuous Solid Electrolyte Interphase (SEI) layer formation, which consumes a large amount of lithium. The SEI is an electrocatalytically inactive compound, which breaks and reforms during charging cycles, consuming the available Li inside the battery, and decreasing the coulombic efficiency of the battery significantly (fig. 1c). The term coulombic efficiency is defined as the ratio of the total charge extracted from the battery to the total charge put into the battery over a full cycle. Both effects, volume expansion an SEI formation ultimately lead to inefficient LIBs. [39]

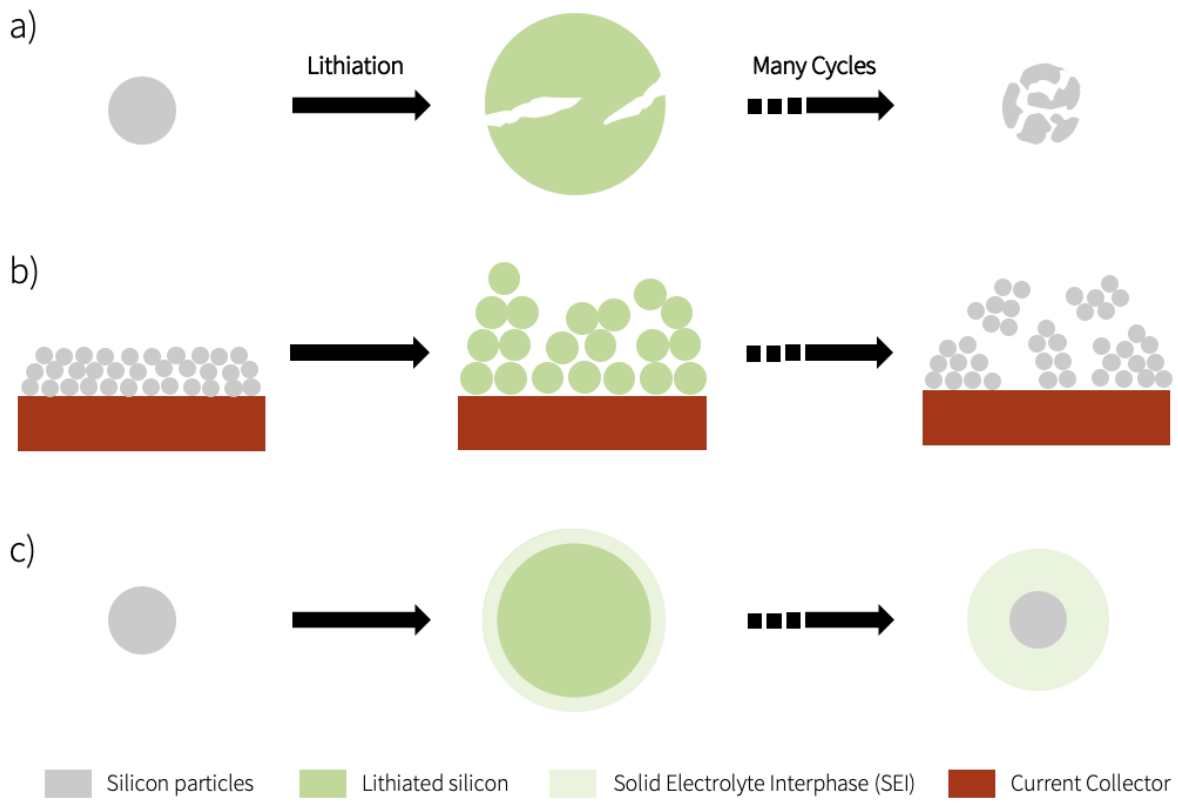

Figure 1: Schematic of silicon anode material failure. a) Cracking of silicon particles due to volume expansion leading to pulverization, b) contact loss of anode material during cycling and c) formation of SEI.

1.4 Strategies for Enhanced Silicon Anode Performance

1.4.1 Nanostructures

Different attempts to find a solution for SEI formation and volume expansion have been made so far. A promising approach is the synthesis of nanosized silicon electrode powders.[40] Reducing particle size under a critical threshold (~150 nm) enhances the mechanical stress resistance during alloying with lithium. The downside of this method is the higher surface-volume-ratio of the material, which offers more area for the SEI formation. Breaking and reforming of electrochemically inactive SEI during charging cycles leads to irreversible capacity loss, even though the nanoparticles are not cracking. High synthesis costs and low tapping densities are also impeding the commercialization of nano-Si as an alternative for anode material of LIBs.[41] Wang *et al.* were the first to apply this technique in 1998. They produced nano-Si/C composite materials by mechanical milling. The electrochemical results indicated higher cycling stability for the synthesised material containing nano-Si than for samples with a larger particle size.[42] In 2012, Liu *et al.* determined the critical cracking size of nano-Si during alloying. They discovered a higher cracking resistance for crystalline nano-Si smaller than ~150 nm and ~870 nm for the amorphous phase via *in situ* TEM.[43] [44]

Not only different particle sizes, but also different morphologies have been proposed with promising results. In 2007, nest-like Si nanospheres prepared via a solvothermal route were proposed. With a first cycle specific discharge capacity of 3952 $mAh.g^{-1}$ at a current density of 100 $mA.g^{-1}$ they clearly outperformed commercial Si particles, which only achieved a capacity of 2600 $mAh.g^{-1}$. Even at much higher charging rates of 2000 $mA.g^{-1}$ they still obtained specific capacities of 3052 $mAh.g^{-1}$. [45] In 2009, Cui *et al.* presented a core-shell design for Si nanowires directly grown on stainless steel in a simple one-step procedure. The material showed a capacity retention of ~90 % after 100 cycles, as well as excellent performance with charging rates 20 times higher than carbon for 1 h (6000 $mA.g^{-1}$).[46]

In the same year Si nanotubes synthesised by reductive decomposition of a silicon precursor in an alumina template followed by etching showed promising results. Specific charge capacity of 3247 $mAh.g^{-1}$ with a coulombic efficiency of ~89 % resulted in a 10 times higher specific capacity than graphite even after 200 cycles. Furthermore, great capacity retention at charging rates as high as 15000 $mA.g^{-1}$ were reported. [47]

1.4.2 Porous Structures

Another promising potential solution is the use of (nano)porous and/or nanostructured silicon materials.[48] [49] The generated pores should provide space to limit the effects of the swelling that occurs during alloying with lithium (fig. 2).

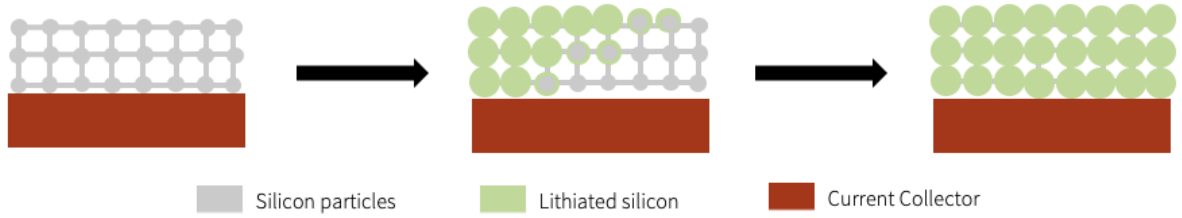

Figure 2: Schematic showing the lithiation of porous Si anode material with smaller Si domains inside battery cell. Pores provide additional space for swollen Li_xSi_y species during alloying with Li from electrolyte species.

Yao *et al.* (2011) investigated the tensile stress hollow and solid silicon nanospheres of the same volume experience during the lithiation process. Hollow structures lower the exerted stress on the nanospheres significantly (83.5 vs. 449.7 MPa for solid nanospheres).[50] In further studies, large mesoporous Si sponges (> 20 µm), which are highly susceptible for cracking during alloying with Li, were synthesised using an electrochemical etching procedure. The work revealed a linear decrease in the porous particle's expansion with increasing void volume during lithiation. For a void volume of 60% they reported a volume expansion ranging from only 75 to 150%, which is an improvement in comparison to 280-400% for bulk Si electrodes.[51] For practical applications as anode materials, porous structures are also favorable, due to higher surface accessibility for the electrolyte. The enhanced ionic diffusion gives the possibility of more capacity availability at higher charging rates. The smaller domains of Si also shorten the Li diffusion length inside the electrode.

Bao *et al.* (2007) were the first to synthesize microporous silicon, using magnesiothermic reduction followed by magnesium removal via acid etching.[52] They started from silica diatom frustules and converted them to MgO/Si replicas (eq. 4). After MgO removal, the specific surface area (SSA) of the particles was increased to 541 m^2g^{-1}.[53] [54] Following this pioneering work, many different porous and/or nanostructured silicon systems were reported in the literature, achieving promising capacities, as well as rate capability and cyclic stability.[55] [56] [57] [58] [59] [60] [61] Unfortunately, high surface accessibility, due to higher specific surface area (SSA), always faces the problem of SEI formation.

1.4.3 Prelithiation

Pretreatment of electrode materials before battery cell operation is an alternative technique to improve LIBs' lifetime. For this procedure, the term of usable capacity is important. It is defined by the reversible transferable Li^+ ions between the cathode and anode materials inside a cell, also called active lithium content (ALC). Materials with high specific capacities, especially cathode materials (e.g., $LiCoO_2$) increase the ALC by serving as a Li ion source in the cell. For anode materials a high amount of Li is lost through SEI formation, especially during the first charging cycle. This significantly lowers the ALC, and therefore the usable capacity of the cell.[62]

The process of prelithiation offers an alternative route for LIBs' anode materials, especially silicon, to avoid irreversible Li^+ ion losses, due to SEI formation. Prelithiation, or pre-doping, of lithium ions is executed by deposition of additional Li in a battery cell before its operation. Increasing the Li content already available inside an anode material helps to counterbalance the ion depletion during cycling. Furthermore, a higher Li content decreases the overall potential of the anode, resulting in an overall higher average potential for the battery cell. [63] [64]

Different techniques are used to obtain anode prelithiation. The most convenient are electrochemically driven lithiation (EDL) and spontaneous corrosion driven lithiation (SCDL) of lithium metal on the anode inside the cell.[65] SCDL is the faster and cheaper prelithiation method of the two since there are no additional setup steps, unlike EDL, which often requires to reopen the battery cell after prelithiation to remove excessive Li.

The effectiveness of both prelithiation methods has already been proven. Kim *et al.* reported a scalable prelithiation scheme based on electrical shorting with Li foil. Their synthesis strategy led to clearly enhanced coulombic efficiencies of 94.9%, 95.7%, and 97.2% in the first three charging cycles. [66] In 2019, Meng *et al.* reported a novel prelithiation procedure with enhanced initial coulombic efficiencies of lithiated SiO_x anodes from 79 to 89% and 68 to 87%. They performed the prelithiation under vacuum conditions, pressing Li foil on the anode after adding an electrolyte and resistance building layer to optimize the process. 200 stable cycles were reported for the as-made anode materials. [67]

1.5 Ordered Mesoporous Silica

A large selection of biological and synthetic silica sources is available as starting material for the reduction of silica to (mesoporous) silicon. Silicas produced from rice husk, diatomaceous

earth, sand, or bamboo silk are just some examples. The silicon synthesis from biological or synthetic silica sources also have certain advantages/disadvantages depending on the used starting material. Silicas produced biologically for example can only be transformed to silicon after the removal of organic impurities. Synthetic silica sources, on the other hand, often consume more energy and resources during synthesis. The right choice of silica starting material plays an important role on how economically or environmentally friendly the production of next-generation battery materials takes place.[68]

Ordered mesoporous silicas (OMS) is one particularly promising example of silica materials for battery applications. Despite the increasing interest in these silicas since their first synthesis by Kresge *et al.* (1992),[69] only few examples of their use as starting materials to produce porous silicon are currently available. Moreover, to the best of our knowledge, all of these studies focused on the use of one type of OMS, SBA-15.[70] This is surprising since OMS are highly tuneable materials, which can be used as starting materials for the synthesis of diverse mesoporous silicon (mSi) anode materials. They can be easily synthesised with tailored pore size, pore architecture, pore volume, and specific surface area (SSA), as well as particle size, shape, and morphology.[71] The versatile synthesis of OMS is possible using amphiphilic surfactants. The self-assembly behaviour (micelle formation) of these molecules determines the meso structure of the resulting silica material. The behaviour of a certain surfactant is described by the surfactant packing parameter g (eq.6):

$$g = V/a_0 l \qquad \text{(eq.6)}$$

where V is the volume of the surfactant's hydrophobic chain, a_0 the effective area of the hydrophilic head group, and l represents the chain length.[72] [73] This behavior is accurate for simple surfactant-in-water systems, where the micelle geometry only depends on the geometry and concentration of the surfactant itself. For OMS synthesis, we have a more complex ternary system of surfactant/water/silicates. Electrostatic interactions or H-bonds between silicates and surfactant have a big influence on the micelle formation and subsequently on the mesostructure of the OMS. [74] The complexity of the ternary system allows the synthesis of structures which cannot be observed in binary systems.[75] Fig. 3 schematizes the synthesis of ordered mesoporous materials based on SBA-15 synthesis procedure. The mesoporous structure is a result of silica condensation directed by self-assembled molecular templates, surfactants, or block-polymers.[76] After solidification of mSi, the volatile organic templates are removed by calcination at high temperatures.

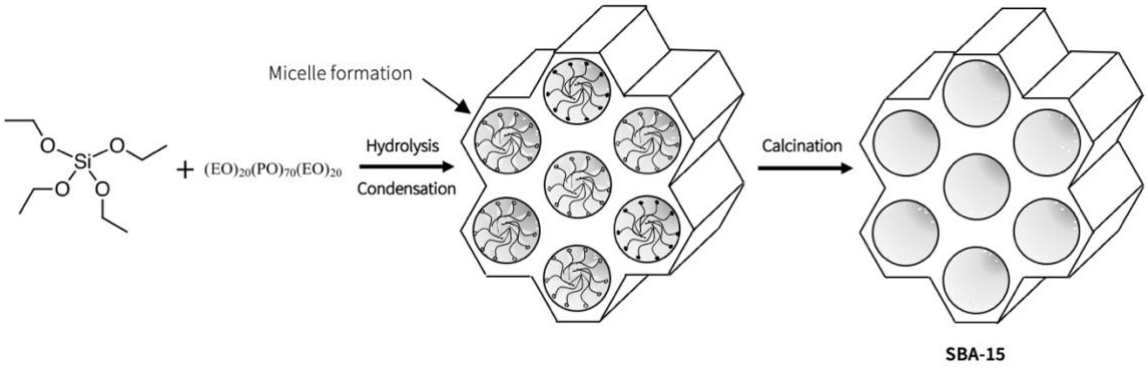

Figure 3: Schemata of SBA-15 pore structure synthesis via micelle formation.

Since 1992 the synthesis of numerous OMS materials, with various structural properties have been reported. All of them can be roughly divided into three categories based on their pore geometry. The first type includes nearly spherical cage pores (e.g., SBA-16 [77] and FUD-12[78]). Hexagonal two-dimensional cylindrical pores are typical for the second category (e.g., MCM-41[79] and SBA-15[80]). OMS materials with bi-continuous pore structure consisting of two interwoven three-dimensional channels separated by a single continuous pore wall belong to third type (e.g., MCM-48 [81] and KIT-6 [82]). In addition to these three categories, other new pore geometries have recently been successfully synthesised. Dendritic mesoporous silica nanospheres (MSNs) are one promising example.[83] Their unique center-radial pore structure with large pore sizes and highly accessible surface areas make this OMS an interesting new candidate for catalysis and biomedical applications.

1.6 Magnesiothermic Reduction

Among the many different methods to synthesize silicon reported in the literature, one of the most convenient is the reduction of silica.[84]. The industrial technique, which involves using silica with carbon in a furnace arc (eq.7), has the downside of a very high reaction temperature (2000°C), which exceeds the melting temperature of silicon (T_m= 1414°C).[85] [86]

$$2\,C\,(s) + SiO_2\,(s) \rightarrow 2\,CO\,(g) + Si\,(s) \qquad \text{(eq.7)}$$

The high reaction temperature leads to the loss of the original particle shape and nano porous silica structure in the resulting silicon. In contrast to carbothermal reduction, magnesiothermic reduction generates silicon under milder conditions of 650°C (eq.8).[87]

$$2\,Mg\,(g) + SiO_2\,(s) \rightarrow 2\,MgO\,(s) + Si\,(s) \qquad \text{(eq.8)}$$

The reaction initiates at even lower temperatures of 540°C and is believed to better preserve the microstructure of the material.[88] Already mentioned in section 1.4.2, Boa *et al.* (2012) used a two-step magnesiothermic reduction procedure for silica reduction. Their method preserved the original particle features, and additionally generated microporous structures by MgO removal via acid etching.[89] In general, for magnesiothermic reduction posttreatments (both HCl and HF etching) are necessary for impurity removal. Besides MgO, magnesium silicide ($MgSi_2$) and minor amounts of magnesium silicate (Mg_2SiO_4) are formed during the reaction (eq.9, 10).[90]

$$2\ Mg\ (g) + Si(s) \rightarrow 2\ Mg_2Si\ (s) \qquad \text{(eq.9)}$$

$$2\ Mg\ (g) + 2\ SiO_2\ (s) \rightarrow Mg_2SiO_4\ (s) + Si\ (s) \qquad \text{(eq.10)}$$

The purity of the resulting material depends on the magnesium to silica ratio which can be adjusted before the reduction. An excess of magnesium ($Mg:SiO_2$ molar ratio = 2.5:1) guarantees a full reduction of the available SiO_2 to silicon, while minimizing the unwanted side reaction of Mg_2Si and Mg_2SiO_4.[91] Besides the stoichiometric factor, Shi *et al.* revealed that lower heating rates also reduce the formation of Mg_2Si and Mg_2SiO_4 for reaction volumes as large as 4 g. They reported reduced heat accumulation with this technique and a significantly lower formation of the unwanted byproducts at the Mg/SiO_2 interface.[92]

A key benefit of the magnesiothermic reduction lies in its versatility, permitting the synthesis of silicon from various silica sources, including OMS. The first magnesiothermic reduction of OMS (SBA-15 nanoparticles) was performed in 2011. Jia *et al.* obtained lotus-root shaped mSi without ordered pore structure. To increase the stability and conductivity of the material, a carbon layer was deposited on the nanoparticles via chemical vapor deposition (CVD). The resulting Si/C composite achieved a specific capacity of 1500 $mAh.g^{-1}$ after 100 charge/discharge cycles at a rate of 1C.[93] Another synthesis route improved the charging cyclability by synthesizing new Si/C nanocomposite morphologies. SBA-15 nanorods were impregnated with carbon precursors, followed by carbonization. 627 $mAh.g^{-1}$ after 220 cycles at 0.1 $A.g^{-1}$ were achieved by the produced particles.[94]

An interesting synthesis protocol to minimize active material loss by volume expansion was introduced by Pan *et al. (*2014*).* Yolk-shell-structured Si/C nanoparticles were synthesised by coating silicon nanoparticles using gas-phase carbon coating, a conventional industrial procedure. An additional sacrificial SiO_2 coating on the silicon surface, which was later removed by HF-treatment provided hollow space for extension during lithiation. At a low

charging rate (0.1 $A.g^{-1}$) the specific capacity was 1938 $mAh.g^{-1}$ after more than 40 cycles.[95] Ashuri *et al.* (2015) published another interesting method of increasing cycling performance of Si/C yolk-shell-structured nanocomposite, through the agglomeration of Si nanoparticles to form pomegranate inspired structures. The pomegranate design reduced the surface area exposed to the electrolyte and therefore reduced SEI formation. Electrochemical results showed good cyclability at a lower charging rate (C/20) with a specific capacity of 2350 $mAh.g^{-1}$ after 1000 cycles.[96]

1.6.1 Heat Modulation

Another key aspect of the magnesiothermic reduction lies in the exothermic nature of the reactions taking place. The formation of MgO (ΔH_f^0= -601.6 kJ/mol_{silica}) significantly increases the heat released during the reduction. The local reaction temperature may even rise above 1000°C. The reactions associated with the formation of undesirable side products, are also very exothermic. Especially Mg_2Si (ΔH_f^0 = -77.8 kJ/mol_{silica}) and Mg_2SiO_4 (ΔH_f^0 = -2174 kJ/mol_{silica}) further increase the heat releasee.[97]

To avoid sintering and other undesirable temperature-related side effects, the generated heat needs to be limited or somehow absorbed/dissipated. One option to realize the idea of heat reduction during the magnesiothermic reaction is the use of a heat modulator with endothermic melting enthalpy. Following this idea, Liu *et al. (*2012*)* obtained silicon nanocrystals from amorphous and crystalline silica sources by magnesiothermic reduction in molten NaCl-$MgCl_2$ or molten LiCl-KCl. Results indicate that the growth of silicon crystals is controllable in the salt melt.[98] Since this synthesis route appeared to lower the porosity of the resulting material significantly (specific surface area = ~120 $m^2.g^{-1}$), Luo *et al. (*2013*)* tried to improve it using a molt of NaCl. The endothermic melting of NaCl (T_m= 801°C, ΔH_{fusion}= ~28.8 kJ/mol) compensated for the heat released during the magnesiothermic reduction, resulting in a milder and more controlled reaction. The starting material, diatomaceous earth, was successfully reduced to silicon while keeping the silica porosity intact.[99] The heat modulation with NaCl to preserve mesostructure also works for larger batches of total reactants (30 g). More material is normally problematic for this reaction, due to the increased heat release. Nevertheless, the NaCl successfully absorbed the released heat and avoided the sintering of particles during reduction.[100]

1.7 LIANO Project

Despite the promising early success of the magnesiothermic reduction process, it is still not clear how efficient this technique is to produce (ordered) mSi starting from OMS. In this project the impact of OMS (nano-)particles' morphology and the use of a heat modulator on the resulting mSi materials for this reduction technique are investigated. Also, new studies on the associated etching treatments are carried out. Detailed characterisation of the obtained mSi materials is executed in order to compare their physio-chemical properties and electrochemical cycling performance with commercial Si nanoparticles as potential next generation silicon anode materials.

The first step of this project includes the synthesis of OMS particles with different particle size, pore size, and pore geometry from precursors via sol-gel-synthesis.[101] [102] [103] [104] Afterwards, magnesiothermic reduction following a traditional synthesis protocol is conducted with the OMS materials. After etching treatments with both HCl and HF, the structure, porosity, and composition of the purified silicon is analysed to see the impact of the three varied parameters on the resulting mSi particles' morphology.
Thermal effects, causing particle agglomeration and ordered pore structure loss led to an adapted synthesis route using NaCl as a heat scavenger.[105], The mSi batches obtained from this procedure are focused on the effects of pore geometry and particle size since pore size doesn't seem to have a significant impact on the resulting materials characteristics. To evaluate the influence of etching steps and impurities in the final product also multiple samples of the same particle type are synthesised and characterised after different progress in the etching posttreatment. Detailed structure, porosity, and composition analysis is performed for all mSi samples synthesised following this protocol. Furthermore, our partners from AIT investigate the electrocatalytic performance and cycling stability of all the final mSi materials during charging/discharging in order to compare common purchasable bulk silicon nanoparticles with our mesoporous alternatives.

As another method to improve the cycling performance of mSi samples three simple methods of silicon prelithiation were tested in the last stage of this thesis' work. Composition analysis indicate that new Li containing phases are obtained by two of the three methods, although oxidation and carbonization of the Li compounds remain a big issue.

2 Materials and Methods

2.1 Synthesis of Ordered Mesoporous Silica

KIT-6, a 3D cubic OMS, was synthesised according to the protocol published by Kleitz *et al.* (2003).[106] The copolymer poly-(ethylene oxide)-block-poly(propylene oxide)-blockpoly(ethylene oxide) (Pluronic P123, $EO_{20}PO_{70}EO_{20}$, Sigma-Aldrich, Germany) was used as the structure-directing agent. In a typical synthesis, 5.13 g of Pluronic P123 were first dissolved in a mixture of 9.93 g concentrated hydrochloric acid (37% HCl, Sigma-Aldrich, Germany) and 185.33 g distilled water. 5.13 g n-butanol (99%, Thermo Fisher Scientific, Germany) were added as a co-structure-directing agent. The mixture was stirred at 35°C until a complete dissolution of the polymer. Then, 11.03 g TEOS (tetraethyl orthosilicate, Sigma-Aldrich, Germany) were added to the solution, followed by stirring at 35°C for 24 h. The homogenous mixture was aged at 40°C or 100°C for 48 h in a convection oven (Binder, Germany), or at 140°C using an autoclave (Berghof, Germany) under static conditions. The procedure for hydrothermal synthesis was adapted from Hochstrasser *et al.* (2020).[107] The resulting white solid product was filtered hot without washing. The silica was dried for 2 h at 100°C and then overnight at 140°C. After the drying was complete, the powder was extracted in a solution of 200 mL of ethanol (96%, Brenntag, Austria) in which 2 drops of concentrated HCl (37%) were added. Finally, the silica material was calcined in air at 550°C (heating ramp ≈ 1.5°C/min) for 3 h.

SBA-15, a 2D hexagonal OMS, was synthesised after a similar procedure [108], but with different formulation and without n-butanol as a co-structure-directing agent. 8.16 g P123 were dissolved in a solution of 149.03 g distilled water and 4.46 g hydrochloric acid (37% HCl). After stirring at 35°C overnight, 13.25 g TEOS were added Further steps were repeated as described in the procedure above for KIT-6 materials.

MCM-48-type-MSNs were synthesised following the protocol of Kim *et al.* (2010).[109] In a typical synthesis, 1.01 g cetyltetramethylammonum bromide (CTAB, Sigma-Aldrich, Germany) and 85.14 mL ethanol were mixed in a plastic bottle as structure directing agents. 4.04 g triblock copolymer F127 (Pluronic F127, $EO_{106}PO_{70}EO_{106}$, Sigma-Aldrich, Germany) were added as particle dispersing agent. Since the synthesis depends on a basic medium, 214.78 mL of an aqueous NH_4OH-solution (2.9 wt.%, Alfa Aesar, Germany) were also added. Under

stirring, the copolymers were dissolved at 25°C for 24 hours. 3.63 g TEOS were added as a silica source under vigorous stirring. After aging at 25°C for 24 hours, the suspension was centrifuged at 10000 rpm for 30 minutes twice, with a washing step after each centrifugation, first in distilled water, then in ethanol. The particles were dried at 70°C in a furnace and calcined in air at 550°C (heating ramp ≈ 1.5°C/min) for 3 h.

For the synthesis of dendritic MSNs, with a radial sponge like pore structure, the reported route of Juére *et al*. (2020*)* was followed.[110] For the aqueous phase, 360 mg triethylamine (TEA, Alfa Aesar, Germany), 8 mL cetyltrimethylammonium chloride (CTAC, 25 wt.% in H_2O, Sigma Aldrich, Germany), and 72 mL distilled H_2O were stirred (150 rpm) at 60°C for 1 h. The organic phase, consisting of 32 mL hexane (Sigma-Aldrich, Germany) and 8 mL TEOS, was added dropwise to the aqueous phase and stirred at 60°C overnight. The organic phase was separated and centrifuged for 30 min at 10000 rpm. After two washing steps in ethanol, the suspension was stirred (700 rpm) in a solution of 100 mL ethanol and 1 drop concentrated HCl (37%) for 2 hours. After another washing step in ethanol, the particles were dried at 100°C in a convection oven overnight. Then, they were calcined in air at 550°C for 5 hours.

2.2 Synthesis of Mesoporous Silicon via Magnesiothermic Reduction

2.2.1 Traditional Synthesis Protocol

The OMS particles were converted to elemental silicon in a tube furnace under a reducing gas atmosphere (95% Ar, 5% H_2). For sample preparation, 700 mg mesoporous silica was powdered with 700 mg elemental magnesium (325 mesh, Alfa Aesar, Germany) under an argon atmosphere and transferred to a MgO-crucible for thermal treatment. The reduction was performed at 650°C for 5 hours with a heating rate of 1.7°C/min. To obtain pure silicon and remove byproducts like MgO, the samples were leached with 2M HCl for 2 hours under stirring and dried at 100°C overnight. The remaining silicon (Mg_2Si, Mg_2SiO_4, SiO_2) was removed by etching in an aqueous HF-solution (10 wt.%, Alfa Aesar, Germany) for 2 h. The end product was washed in 500 mL ethanol and distilled H_2O and dried at 70°C overnight. Table 1 gives an overview of the first silicon samples. Samples were denoted as a function of the OMS used. S for SBA-15, K for KIT-6, M for MCM-48-type, and D for dendritic MSNs.

Table 1: Description of sample labelling for samples synthesised via the traditional protocol.

	Silica Particle	
Sample	Type (Pore Geometry)	Aging T [°C]
S1	SBA-15	100
S2	SBA-15	140
K1	KIT-6	100
K2	KIT-6	140
M1	MCM-48-type MSNs	N/A
D1	Dendritic MSNs	N/A

2.2.2 Adapted Synthesis Protocol

The harsh reaction conditions required an adaption of the magnesiothermic reduction process. Samples were impregnated the samples with sodium chloride (NaCl, Alfa Aesar, Germany) before reduction to reduce the morphology changes due to the released heat. Therefore, a molten-salt protocol of Liu *et al.* (2012) was followed.[111] 700 mg mesoporous silica was suspended in an aqueous solution of 7 g NaCl in 20 mL distilled H_2O. After stirring at 60°C for 1 hour, the H_2O was evaporated slowly first in the convection oven at 100°C for 2 hours, then in the vacuum oven at 150°C. The mixture of salt and silica was then used for the magnesiothermic reduction described as above. Not all of the samples were fully etched in order to observe the impact of HCl and HF treatment on the resulting material. Samples that underwent the etching procedure with HCl were etched 2 times for 2 hours each, to improve the purity of the final products. The samples impregnated with NaCl before reduction and the applied etching post-treatment are listed in table 2:

Table 2: Description of sample labelling for samples synthesised via the adapted heat scavenger protocol.

	Silica Particle		Etching Treatment	
Sample	Type (Pore Geometry)	Aging T [°C]	HCl	HF
S3	SBA-15	100	Yes	Yes
S4	SBA-15	100	Yes	No
S5	SBA-15	100	No	No
K3	KIT-6	100	Yes	Yes
K4	KIT-6	100	Yes	No
K5	KIT-6	100	No	No
M2	MCM-48-type-MSNs	N/A	Yes	Yes
M3	MCM-48-type-MSNs	N/A	Yes	No
M4	MCM-48-type-MSNs	N/A	No	No
D2	Dendritic MSNs	N/A	Yes	Yes
D3	Dendritic MSNs	N/A	Yes	No
D4	Dendritic MSNs	N/A	No	No

2.3 Prelithiation of Mesoporous Silicon

To reduce the capacity loss of the silicon electrode material during forming an alloy with lithium, three different prelithiation processes were tested on the silicon material made from KIT-6-100. The most promising method was used for prelithiation of the remaining samples.

For the first method, the procedure of Betz *et al.* was followed.[112] 50 mg mSi and 3 mg lithium stearate (Alfa Aesar, Germany) were hand-milled for ~10 min and transferred to a MgO-crucible. In a tube furnace, the mixture was heated to 300°C at a heating rate of 5°C*min^{-1} and kept at this temperature for 4 h. After cooling to room temperature, the material was hand milled again for 10 min.

The second prelithiation strategy was adapted from Scott *et al.*.[113] and performed by suspending 50 mg silicon in 10 mL cyclohexane (Sigma-Aldrich, Germany) in the glovebox ($H_2O \leq$ 0.1ppm, $O_2 \leq 0.1$ ppm). 2 mL n-butyllithium (n-BuLi, Sigma-Aldrich, Germany) was dropped into the suspension, which was then stirred (700 rpm) for 24 hours under argon atmosphere.

To remove cyclohexane the samples were dried first at 100°C under air for 1 hour and then at 150°C under vacuum for 2 hours.

Finally, a physical impregnation route adapted from Li *et al.* was tested.[114] 50 mg mSi was mixed with 39 mg elemental lithium (99%, Acros Organics, Germany) under an inert atmosphere. After hand milling three times for 10 minutes each, the mortar was washed with cyclohexane to remove the product. The wet product was dried in an oven at 100°C for 2 hours. In total, 10 samples have been prelithiated following one of the three procedures as table 3 shows:

Table 3: Sample labelling for prelithiated samples.

		Silica Particle		Etching Treatment	
Sample	Prelithiation Method	Type (Pore Geometry)	Aging T [°C]	HCl	HF
L1a	1	KIT-6	100	Yes	Yes
L1b	2	KIT-6	100	Yes	Yes
L1c	3	KIT-6	100	Yes	Yes
L2	2	SBA-15	100	Yes	Yes
L3	2	Dendritic MSNs	N/A	Yes	Yes
L4	2	MCM-48-type-MSNs	N/A	Yes	Yes
L5	2	KIT-6	100	Yes	No
L6	2	SBA-15	100	Yes	No
L7	2	Dendritic MSNs	N/A	Yes	No
L8	2	MCM-48-type-MSNs	N/A	Yes	No

2.4 Materials Characterization

The pore structure and textural properties of the samples were analysed using N_2 physisorption isotherms measured at −196°C on an Anton Paar Quantatech Inc. iQ2 and iQ3 instrument (Boynton Beach, Florida, USA). Prior to analysis, 100 mg of each sample was outgassed under vacuum at 150°C for 12 h. Specific surface area (SSA) was calculated using the Brunauer−Emmett−Teller (BET) equation applied to data points measured in the relative pressure range $0.05 \leq P/P_0 \leq 0.3$. Pore size distributions and total pore volume were calculated from both the desorption and adsorption branches of the isotherms by applying the non-local

density functional theory (NLDFT) considering an amorphous SiO_2 surface and a cylindrical pore model. The calculations were carried out using the ASiQwin 5.2 software provided by Anton Paar Quantatech Inc.

X-ray diffractograms were recorded on a PANalytical EMPYREAN powder diffractometer equipped with the PIXcel3Ddetector (Malvern PANalytical, United Kingdom) in reflection geometry (Bragg–Brentano HD) using Cu Kα ½ radiation, operated at a voltage of 45 kV and a tube current of 40 mA, with a fixed divergence slit of 0.05 mm. Low-angle diffraction data were collected in transmission geometry (Focusing Mirror). Measurements were performed in continuous mode with a step size 2θ of 0.013° and a data time per step of 300 s (reflection) or 50 s (transmission). A MACOR sample holder and a linear position-sensitive detector LynxEye with the following parameters: opening of 2° 2θ and resolution ~0.01° of 2θ, were used.

(High-Resolution) Transmission Electron Microscope ((HR-)TEM) images were taken on Philips CM200 and JEM3010 microscopes at an accelerating voltage of 300 keV using suspensions of the synthesised particles in ethanol deposited on a carbon-copper grid. ImageJ® software was further used to check the particle sizes of MCM-48-type and dendritic MSNs. Scanning electron microscopy (SEM) was conducted on a ZEISS Supra 40 microscope at an accelerating voltage of 3 keV.

2.5 Electrochemical Analysis

Si/C composite electrodes were prepared by water-based processing. Sodium carboxymethyl cellulose (CMC, Mw~250000, Sigma Aldrich) and Poly(acrylic acid) (PAA, Mw~450000, Sigma Aldrich) were used as binder materials and dissolved in a 1:8 vol./vol. mixture of isopropanol and water. After complete dissolution, Super C45, the synthesised Si materials, and TIMCAL C-NERGY™ KS 6L were added working as conducting agent (CA), graphite (C), and silicon (Si) active materials, respectively. A relative ratio of C:Si:CA:CMC:PAA of 85.5:9.5:1:2:2 was targeted. Each addition of one component was followed by manual homogenization in an agate mortar. Finally, the obtained slurries with 30-40 wt.% solid contents were cast on Cu foil (14 µm thickness) using a doctor blade with a gap size of 120 µm, targeting active material loadings of 3-4 mg/cm². The cast electrodes were dried in a vacuum furnace for at least 16 hours at 100°C. Then circular shapes (15 mm diameter) were

cut from the electrode sheets and again dried at 120°C under vacuum before storing them in an Ar-filled glovebox ($H_2O \leq 0.1$ppm, $O_2 \leq 0.1$ ppm) prior to use.

Coin cells were assembled inside the Ar-filled glovebox using 2016 cell casings. A polypropylene separator (Celgard 2500) and 50 µl of carbonate electrolyte (1M $LiPF_6$ in ethylene carbonate:ethyl-methyl carbonate (EC:EMC = 3:7 vol./vol.). Additionally, 2wt.% vinylene carbonate (VC), Soulbrain) and 5 wt.% fluoroethylene carbonate (FEC, Sigma Aldrich) were added to the electrolyte. Furthermore, one stainless-steel spacer (0.4 mm thick) and a steel spring were added to ensure good electrical contact.

Constant current constant voltage (CCCV) testing of the electrodes was executed using a Maccor Series 4000 battery cycler. All tests were conducted within a potential rage of 0.05 - 1.0 V (vs. Li/Li+ counter). The constant voltage (CV) step was held until the current fell below 6.5 $mA.g^{-1}$ (~C/100). The cycling procedure for the assembled cells was as follows: after a 2-hour relaxation step, 2 cycles at 32 $mA.g^{-1}$ (~C/20) were performed for initial formation of the cells, followed by cycling with either 325 $mA.g^{-1}$ (around C/2) or 65 $mA.g^{-1}$ (~C/10).

3 Results

3.1 Characterisation of Ordered Mesoporous Silica

The first step to obtain the desired mSi anode materials is the synthesis of OMS starting materials via reproducible and accurate methods. [115] [116] [117] [118]. In this work, 3D-ordered mesoporous KIT-6 and 2D-hexagonal SBA-15 aged at different temperatures is used. Additionally, MCM-48-type MSNs and dendritic MSNs, two siliceous materials with particle size in the nano range (~150 nm), are used to define the impact of the particle size. Dendritic MSNs also have an additional, interesting pore structure (i.e., a sponge like structure). The mesoporous ordering of produced silica materials, as well as particle size of nanoparticles are verified by low-angle-XRD measurements and TEM images. For dendritic MSNs, only N_2 at 77K physisorption analysis was performed since the complex and amorphous pore structure of the material doesn't show a typical pattern in the low-angle XRD region.

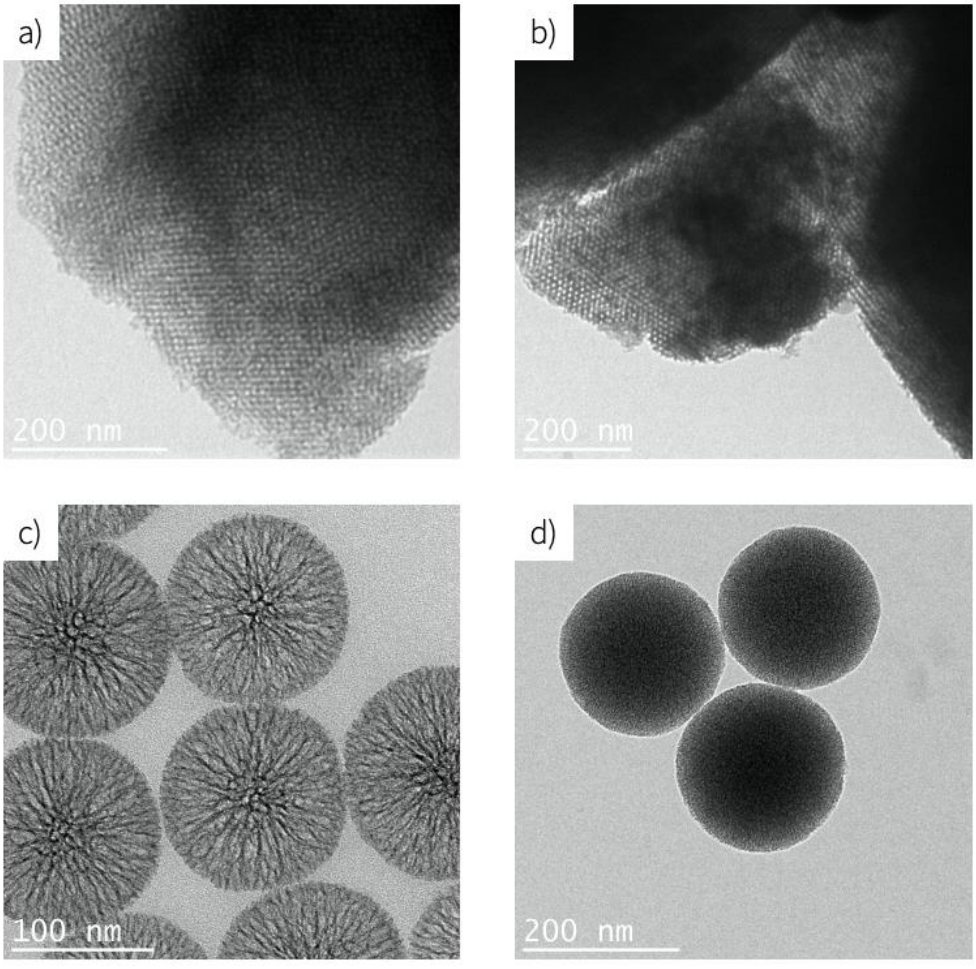

Figure 4: TEM images of OMS materials. a) KIT-6, b) SBA-15 bulk materials synthesised at 100°C, c) dendritic MSNs (150 nm) and d) MCM-48-type MSNs (150 nm).

Figure 4 shows TEM-images of the highly ordered structure of the 4 OMS materials synthesised, which confirms the synthesis was successful. Furthermore, for nanoparticles the desired diameter around 150 nm is achieved (fig. 4). The low-angle-XRD measurements present reflection patterns typical for the ordered pore structure of the synthesised materials. Reflections at $2\theta = 0.9°$ and 1.7° of the 211 and 220 are detected, characteristic of the 3D KIT-6 body-centered cubic Ia3d space group. SBA-15 bulk materials show 100 (2θ = 0.9°), 110 (1.4°), and 200 (1.7°) reflections from two-dimensional hexagonal mesopores with an average pore size of 8.5 nm. 211 and 220 reflections at $2\theta = 2.8°$ and 3.2° for the MCM-48-type MSNs confirm the same space group as KIT-6 material with a smaller pore size around 3.5 nm (fig. 5a-c).[119 120]

The N_2 physisorption isotherm of dendritic MSNs (fig. 5d) shows the two for this material characteristic hysteresis loops. The first appears at lower relative pressures (p/p0 = 0.60-0.80) and results from the pore size in the mesoporous range. The second hysteresis (p/p0 = 0.95-1.00) originates from interparticle adsorption. Consequently, the results confirm the successful synthesis of sponge like porosity.

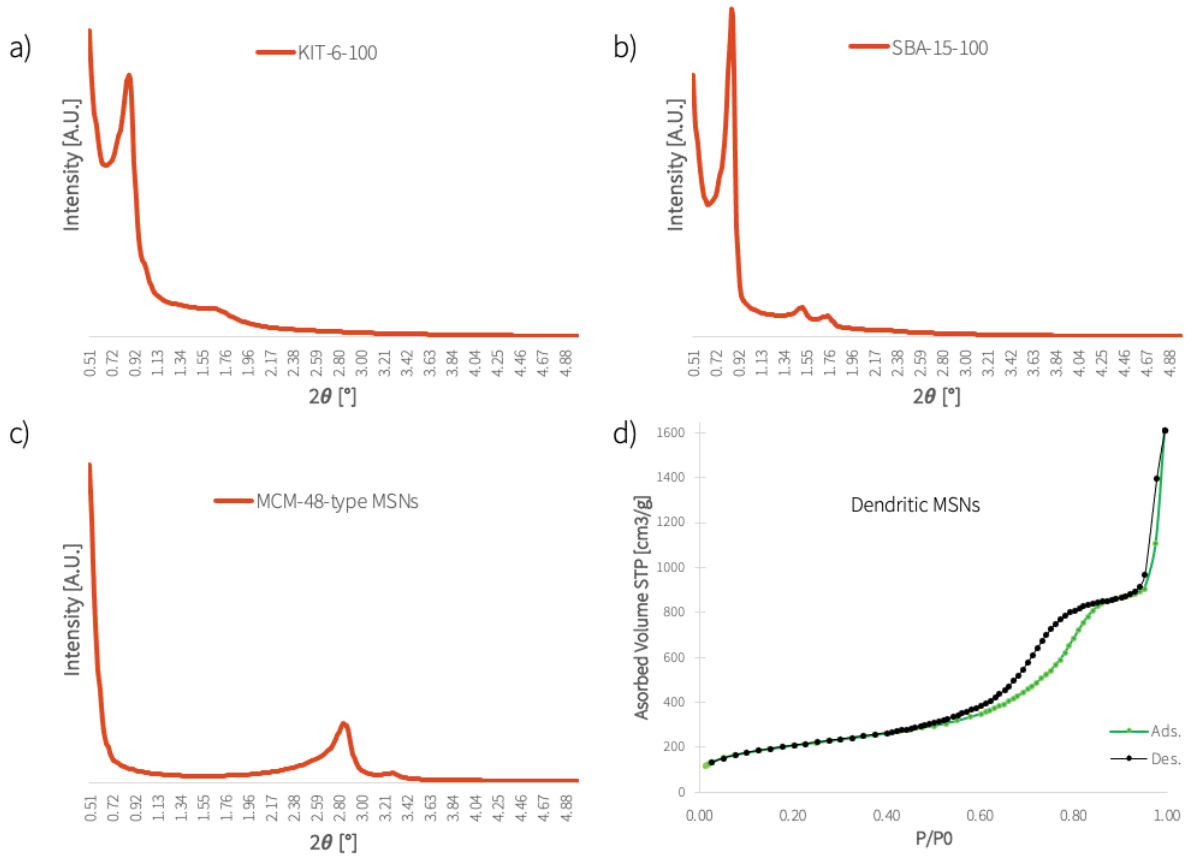

Figure 5: low-angle XRD patterns of a) KIT-6-100, b) SBA-15-100, and c) MCM-48 silica materials. d) typical N_2 physisorption isotherm of Dendritic MSNs measured at 77K.

3.2 Traditional Reduction Protocol Materials

3.2.1 Pore Structure and Surface Analysis

All samples synthesised via traditional magnesiothermic reduction remain relatively porous with BET specific surface areas between 80-280 m^2/g and pore volumes ranging from 0.09-0.55 cm^3/g (table 4). The pore volumes include only mesopores to provide a better indicator of how much of the mesoporous structure is preserved after the reduction. Mode pore sizes range from 5 to 14 nm, which correlate to the pore size of the OMS starting materials. In general, the nanoparticles' pores enlarge during reduction, due to interparticle space occurring during particles sintering process. For dendritic MSNs the pore size increases from 7.5 nm to 13.9 nm and for MCM-48-type MSNs an enlargement from 3.5 nm to 5.1 nm is measured. For the bulk materials only, K2 made from KIT-6 aged at higher temperature show larger mode pore size after reduction compared to the starting material. S1, K1, and S2 have smaller pore size averages, an indicator of melted ordered pore structure.

Further insights on the pore structure of the OMS starting materials are provided by their N_2 isotherms measured at 77K (fig. 6). As expected for mesoporous materials, isotherms of the type IV(a) were obtained for all silicas. MCM-48-type MSNs should have a fully reversible type IV(b) isotherm due to their narrow uniform pores smaller than 4 nm. Nevertheless, the materials shows small hysteresis at high relative pressures (p/p0 = 0.95 -1.00) originating from interparticle voids.[121] Silica bulk materials KIT-6 and SBA-15 are characterised by H1 hysteresis, typical for narrow range pores where networking effects are minimal. As mentioned above, dendritic MSNs show 2 isotherm hysteresis originating from the uniform pore sizes and the adsorption in interparticle space.

After magnesiothermic reduction, no Si material shows the same hysteresis as their silica parent material, which suggests the loss of the highly uniform pore structure during reduction. Again, isotherms of the type IV(a) indicate mesoporous structures, but hysteresis of H3 or H4 type are typical for a more complex porosity, with broader pore size distributions and network effects spanning the whole mesopore range.[122] Even though the uniform pore width can't be maintained, the silicon materials' isotherms demonstrates the presence of mesopores after the reaction.

Table 4: Specific surface area, NLDFT pore volume up to 50 nm, and mode pore size of the silicon materials.

sample		BET specific surface area [m²/g]	NLDFT pore volume up to 50 nm [cm³/g]	NLDFT mode pore size [nm]
mSi (SBA-15-100)	S1	156	0.41	6.8
mSi (SBA-15-140)	S2	189	0.49	7.0
mSi (KIT-6-100)	K1	278	0.55	7.1
mSi (KIT-6-140)	K2	79	0.22	11.7
mSi (Dendritic MSNs)	D1	149	0.47	13.9
mSi (MCM-48-type-MSNs)	M1	130	0.24	5.1

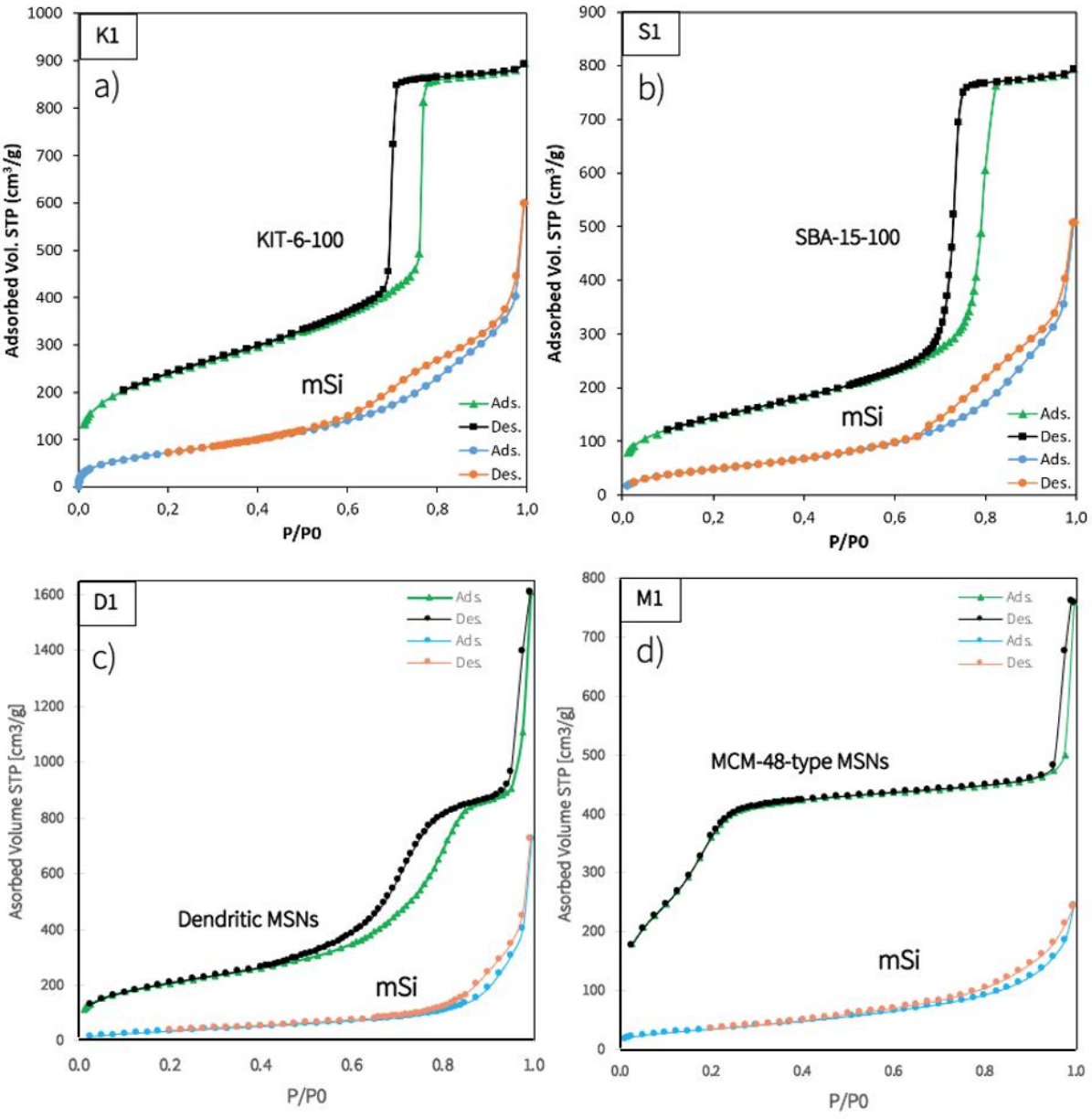

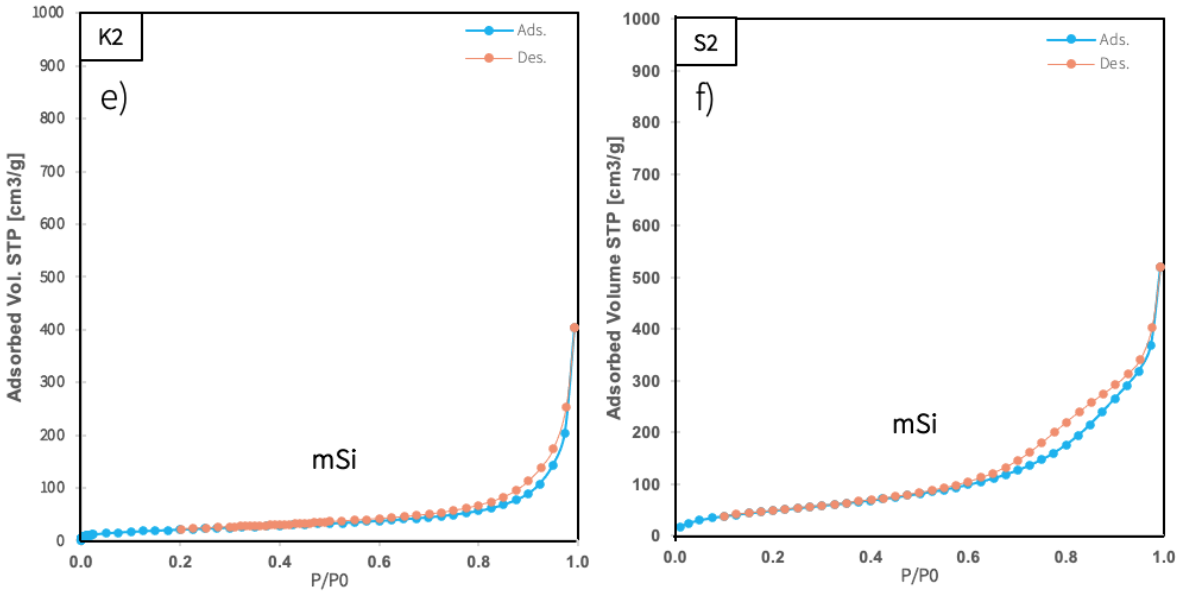

Figure 6: N_2 at 77K physisorption isotherms measured at 77K of the OMS species (a-c) and of the mSi samples synthesised via traditional magnesiothermic reduction protocol (a-f).

The comparison of low-angle-XRD patterns of silica materials from fig. 5 with the patterns from mSi samples from fig.7 shows, that peaks resulting from highly ordered pore structure are missing for mSi samples. No reflections in the low-angle area further confirm the loss of uniform pore size and pore structure, most likely due to sintering/thermal effects. The results from XRD also correlate with the H3 and H4 hysteresis of N_2 isotherms from these materials, indicating a more heterogeneous pore size distributions after the reduction process.

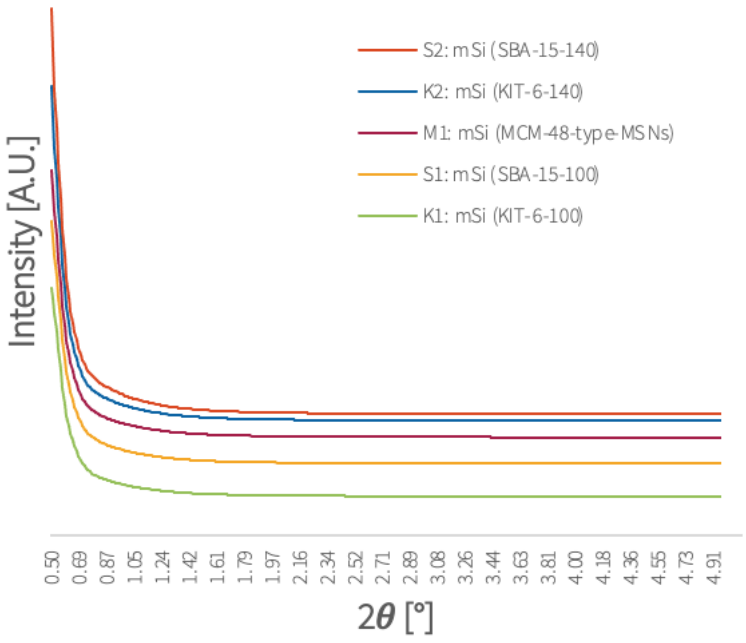

Figure 7: Low-angle XRD reflections of fully etched samples synthesised via traditional magnesiothermic reduction protocol.

The nanostructure, especially the pore structure and particle morphology of the mSi materials is exposed by TEM imaging (fig.8). Mesopores are still observed, but the order is clearly lost. Also, the particle size and shape changed dramatically. Particles are sintered together and form agglomerations. TEM images of the nano-Si material M1 made from MCM-48-type MSNs show that especially nanoparticles are affected. The shape of the original silica nanoparticles can still be seen inside the clustered mass, confirming the theory of particles sintering together during the magnesiothermic reduction. Furthermore, new voids in the mesoporous area have emerged within the formed agglomeration.

SEM-images of mSi synthesised following the traditional reduction protocol give a better overview over the dimension of the sintering effects (fig. 9). Independent on the used OMS starting material, the surface structures look similar for all mSi products. The resulting silicon material consists of particle agglomerations several microns in size. Mesopores can still be seen in between the clusters. The origin of the pores seem to be interparticle voids that are embedded into the (nano-)particles agglomerations.

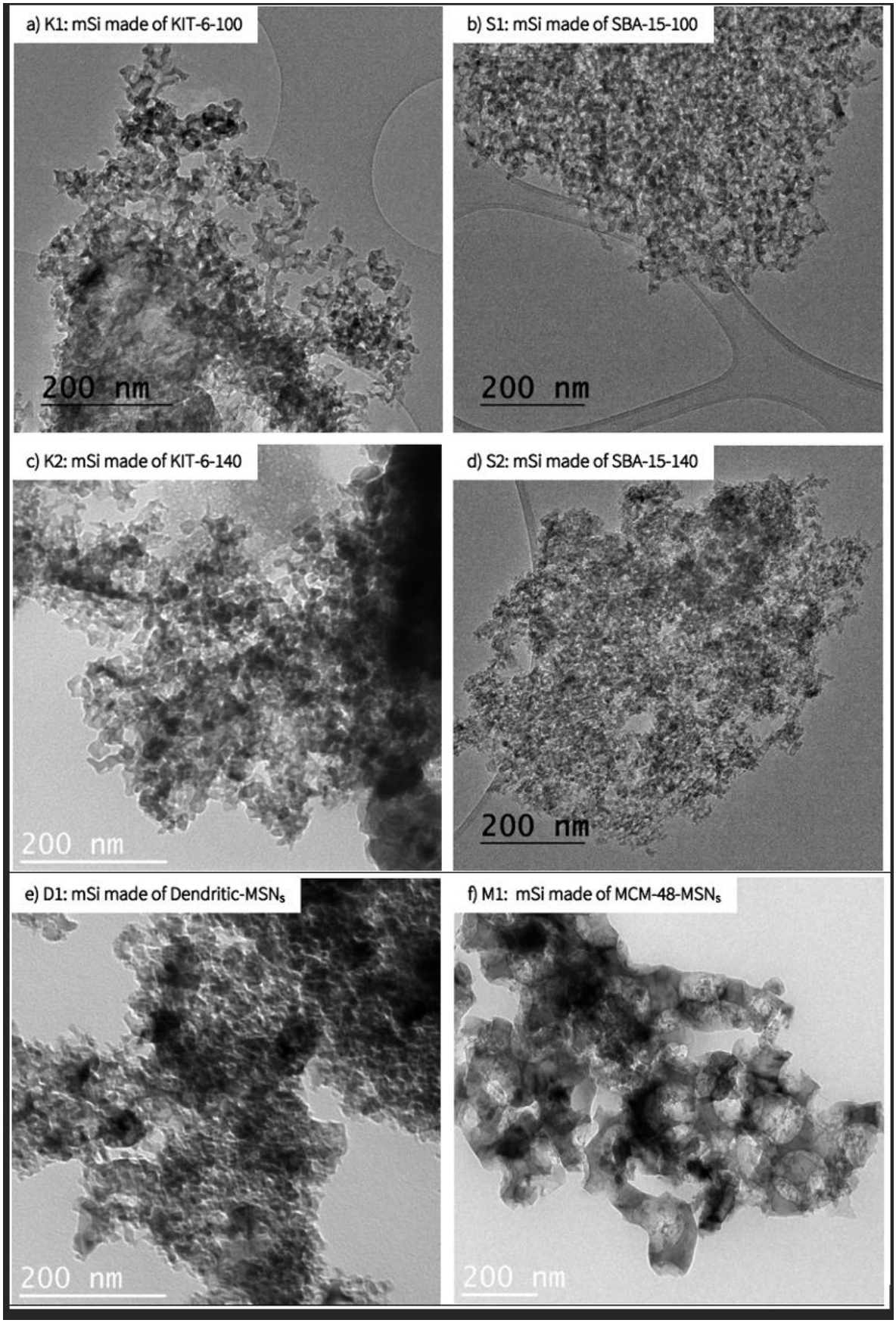

Figure 8: a-f) TEM images obtained for mSi samples made from different starting ordered mesoporous silica materials.

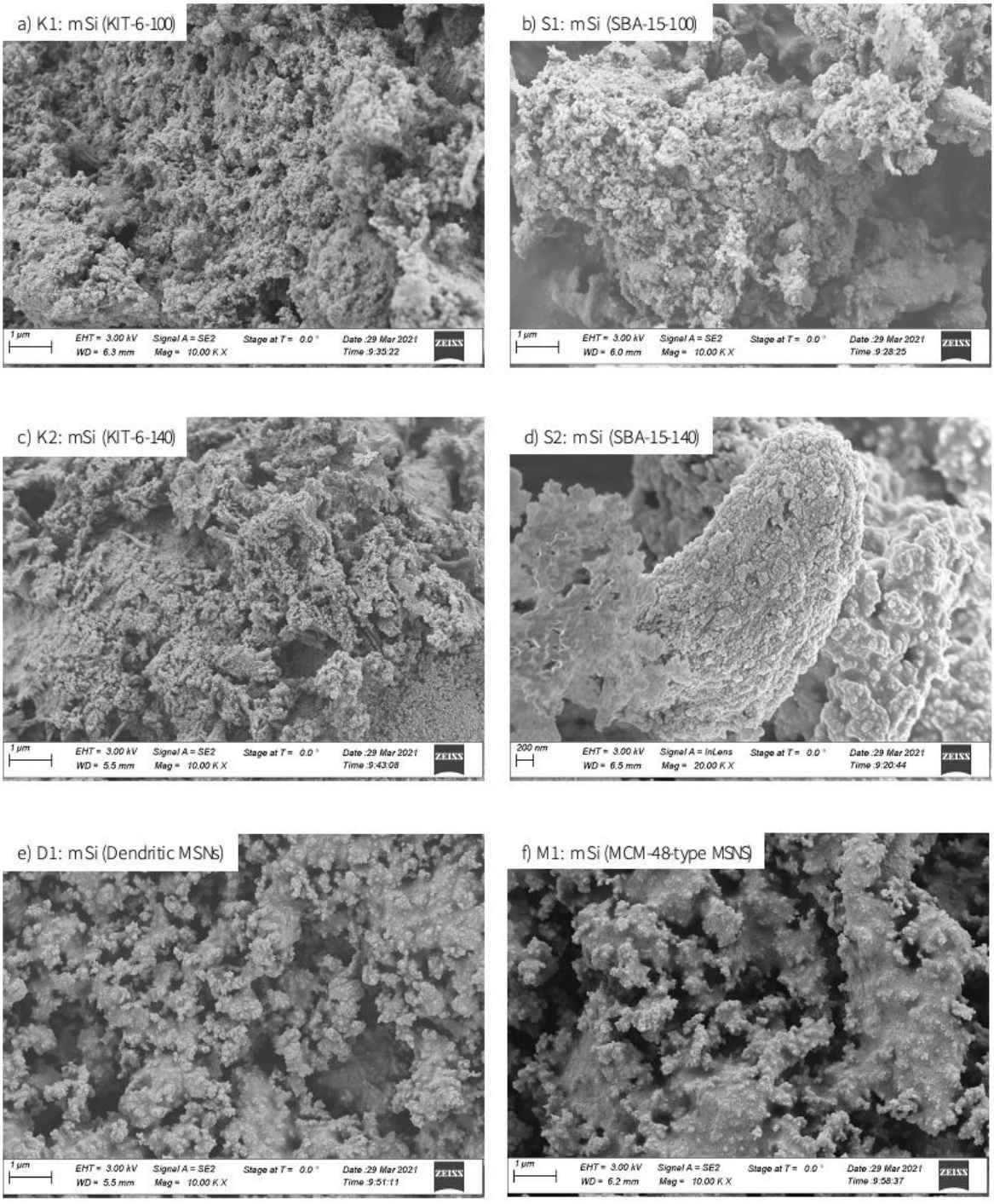

Figure 9: SEM images of as-made mSi samples prepared from a,c) KIT-6, b,d) SBA-15 materials synthesised at 100°C and 140°C, e) dendritic MSNs, and f) MCM-48-type MSNs synthesised via traditional reduction protocol.

3.2.2 Composition Analysis

The conversion of mesoporous silica (nano-)particles to silicon and the purity of the product in general was investigated via wide-angle-XRD (fig. 10). Samples synthesised without a heat scavenger consist of almost phase pure silicon with only small impurities. Reflections at 2θ = 17° for all samples except K1 indicate the existence of amorphous $Mg(OH)_2$. Also, sample M1 shows a reflection at 2θ = 40° and 53°, an indicator of incorrect reaction stoichiometry, which results in Mg_2Si formation. Furthermore, samples M1, S2, and K1 show small peaks at 2θ = 44°, resulting from the 200 reflection of MgO.[123]

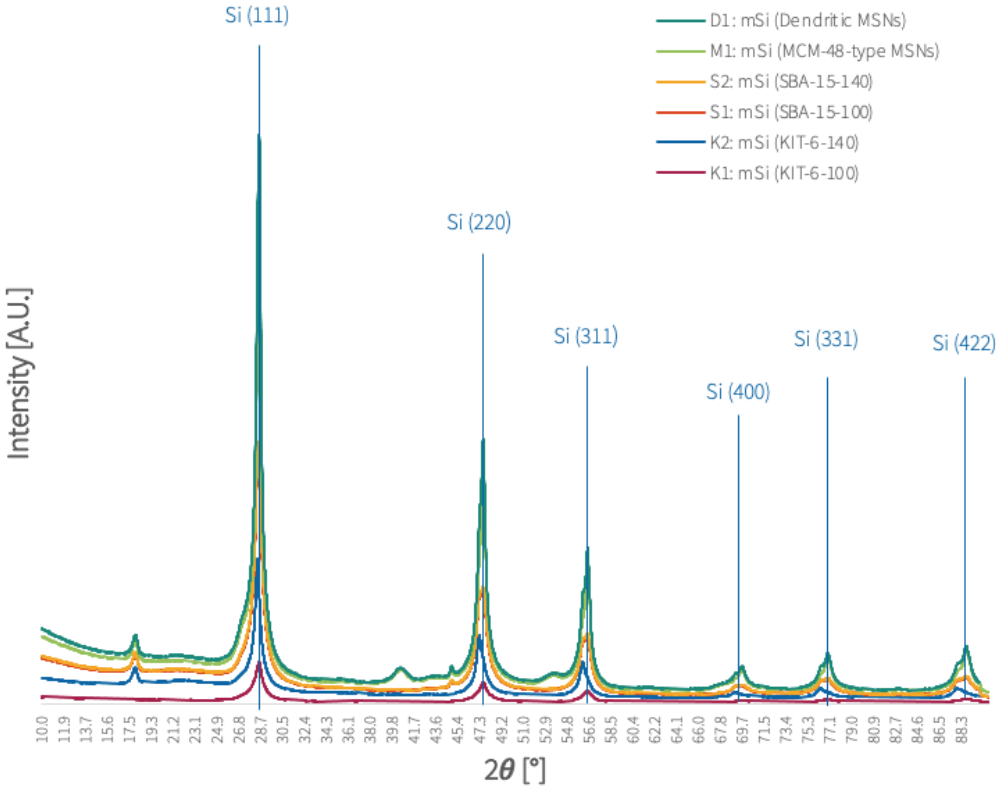

Figure 10: wide-angle XRD patterns of silicon samples synthesised without the use of NaCl as a heat scavenger during synthesis.

3.2.3 Electrochemical Analysis

Electrodes made from the prepared silicon materials are evaluated for cycling performance and first cycle coulombic efficiency. Due to the high volumetric changes of the silicon during the discharge/charge process, the materials cannot be used alone as an active species in an electrode. Silicon/graphite (Si/C) composite electrodes are prepared. Here, the relative amount

of silicon is fixed to 10 wt.% for all samples. Two commercial silicon nanoparticle powders with different particle sizes (30-50 nm and 130 nm) are used as reference materials.
The two reference electrodes deliver specific charges of about 600 $mAh.g^{-1}$ (30-50 nm particles) and 400 $mAh.g^{-1}$ (130 nm particles). Compared to pure graphite (350 $mAh.g^{-1}$) the specific charge increase corresponds to 250 $mAh.g^{-1}$ and 50 mAh.g-1, respectively. The high electrochemical performance of the electrodes prepared with the smaller Si nanoparticles (30-50 nm) can only be maintained using electrolyte additives (fluoroethylene carbonate, FEC). However, the additive is consumed during the discharge/charge processes and a sharp drop in specific charge could be observed after only about 40-50 discharge/charge cycles.

Electrodes prepared with synthesised mSi alternatives achieve similar specific charge values of up to 550 $mAh.g^{-1}$ (M1 made from MCM-48-type MSNs). The material benefits from the nanosized particles (150 nm), which lead to higher stress resistance. The dendritic MSNs, which should also profit from their size (150 nm) don't show the same enhancements in performance. Dendritic MSNs only have 150 $mAh.g^{-1}$ higher specific charge values, like the bulk materials. The cycling stabilities were little different from the electrodes fabricated with the reference materials, and similarly, the high initial specific charges could be stabilized only by adding FEC to the electrolyte. The consumption of FEC and subsequent sharp drop in the achievable specific charges occurred sooner in electrodes containing the mSi (~70 cycles) compared to the reference materials, finally leading to total electrode failure between 80 and 90 cycles (fig. 11).

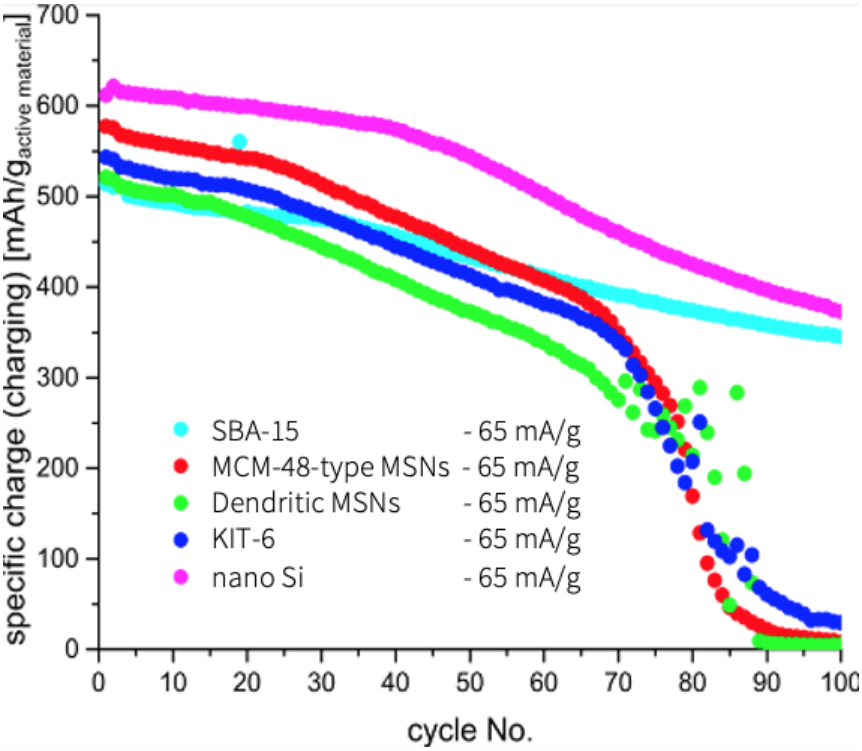

Figure 11: cycling performance for Si/C composite anodes using Si nanoparticles and samples synthesised via traditional reduction protocol.

The 1st cycle coulombic efficiencies show that less Li is used during the initial SEI formation for electrodes prepared using the reference Si nanoparticles compared to the mSi synthesised following the traditional reduction protocol. The higher consumption of Li makes sense since porous (nano-)particles tend to increase SEI formation during first cycling due to a higher SSA. Electrodes prepared with the smaller reference nanoparticles (30-50 nm) have the highest 1st cycle coulombic efficiencies of the investigated silicon (nano-)particles with 86%. Materials made from MCM-48-type MSNs again profit from their small size. 79% of the total charge put into the battery is extracted again after the 1st cycle.

Electrodes with purchasable 130 nm nanoparticles retain 77% of their total charge over the 1st cycle, while those with dendritic MSNs only have coulombic efficiencies of 74%, likely due to the high porosity of the sponge-like particles. Bulk materials made from KIT-6 and SBA-15 retain slightly lower efficiencies between 73 and 77% (fig. 12).

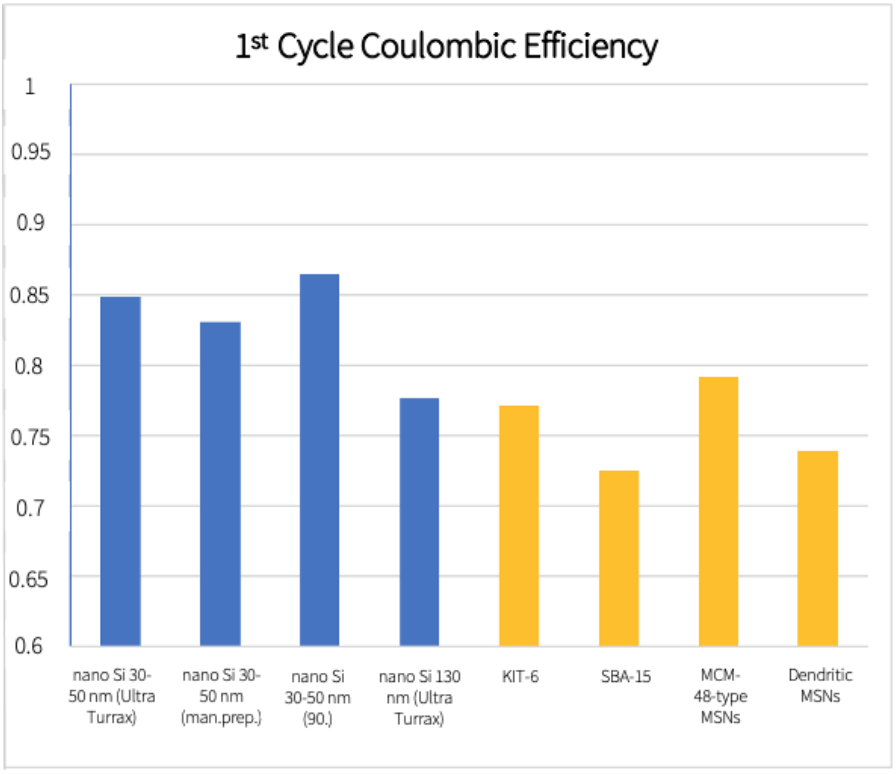

Figure 12: 1st cycle coulombic efficiencies for Si/C composite anodes using Si nanoparticles and samples synthesised via the traditional reduction protocol.

3.3 Adapted Reduction Protocol Materials

The results from samples synthesised following the traditional magnesiothermic reduction indicate that the reduction is still too harsh. A new protocol that includes the use of a heat scavenger (NaCl, present in excess) during reduction is used to minimize the heat-induced morphological and structural damage.[124] The new method is not applied to KIT-6 and SBA-15 materials synthesised under hydrothermal conditions (140°C), since the slightly larger pore size of the materials doesn‘t improve the quality of the resulting mSi anode material. Furthermore, a smaller number of starting materials moves the focus of the work even more on the benefits of heat modulation, different pore morphologies and particle size.

3.3.1 Surface and Pore Structure Analysis

Physio-chemical properties of the mSi samples synthesised via adapted reduction protocol and samples subjected to classic magnesiothermic reduction synthesis route are comparable. Specific surface areas between 100-180 m^2/g and pore volumes between 0.40-0.75 cm^3/g in the mesopore region are lower than for samples synthesised via the traditional reduction route. The pore size averages range from 5 to 22 nm (table 5). For mSi made from SBA-15-100, the

pore size decreases during reduction, probably due to melting of the material's original structure. For the MCM-48-type particles, pore size significantly increases from 3.5 nm to 22 nm, which again can be indicator of the creation of interparticle spaces due to the sintering of nanoparticles during reduction (table 5).

Type IV(b) N_2 isotherms confirm mesoporosity of the silicon materials, but the H3 type hysteresis loop and low-angle XRD patterns indicate a more complex mesostructure and the loss of ordered pore structure after the heat modulated reduction for all 4 samples (fig. 13).

TEM images similar to the images of samples synthesised via traditional protocol confirm that the ordered pore structure of the original silica materials is lost (fig. 14a-d). Even with the use of a heat scavenger during the reduction, the particles still agglomerate. Again, particularly the nanoparticles are affected. Also, the already addressed interparticle spaces can be seen inside the clusters of particles.

SEM imaging further exposes large areas of clustered particles after reduction. For Dendritic and MCM-48-type MSNs, the original shape of the spherical nanoparticles can still be observed on the images.

Table 5: Specific surface area, NLDFT pore volume up to 50 nm, and mode pore size of silicon materials synthesised via the adapted reduction protocol.

sample		BET-surface area [m^2/g]	NLDFT pore volume up to 50 nm [cm^3/g]	NLDFT mode pore size [nm]
mSi (KIT-6-100)	K3	129	0.67	22.0
mSi (SBA-15-100)	S3	177	0.41	4.5
mSi (Dendritic MSNs)	D2	149	0.41	18.6
mSi (MCM-48-type-MSNs)	M2	99	0.75	22.1

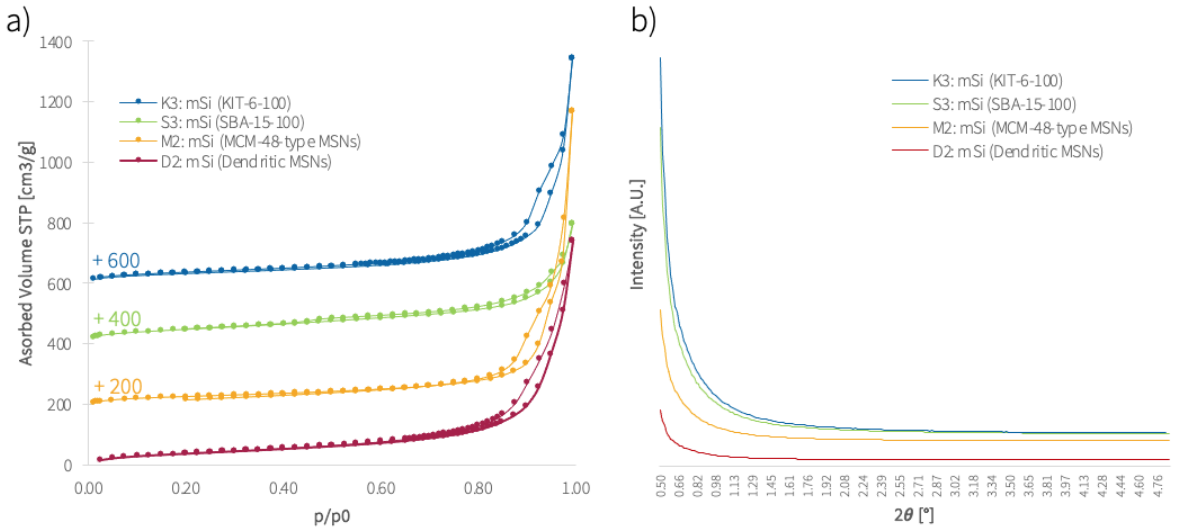

Figure 13: a) N_2 physisorption isotherms measured at−77K b) low-angle XRD reflections of fully etched samples synthesised via the adapted heat scavenger reduction protocol.

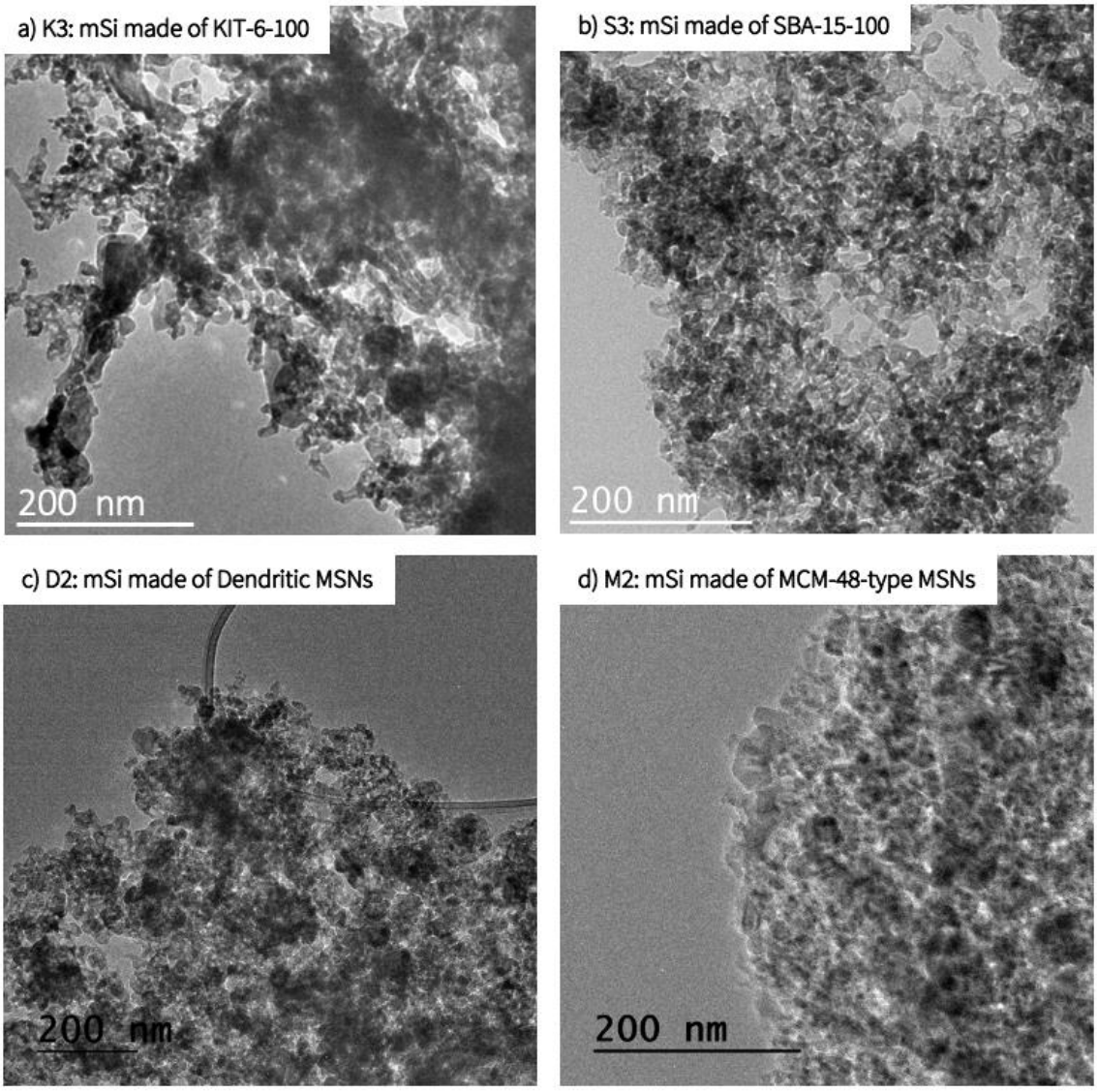

Figure 14: a-d) TEM images obtained for mSi samples made from different starting OMS materials and reduced via adapted heat scavenger protocol.

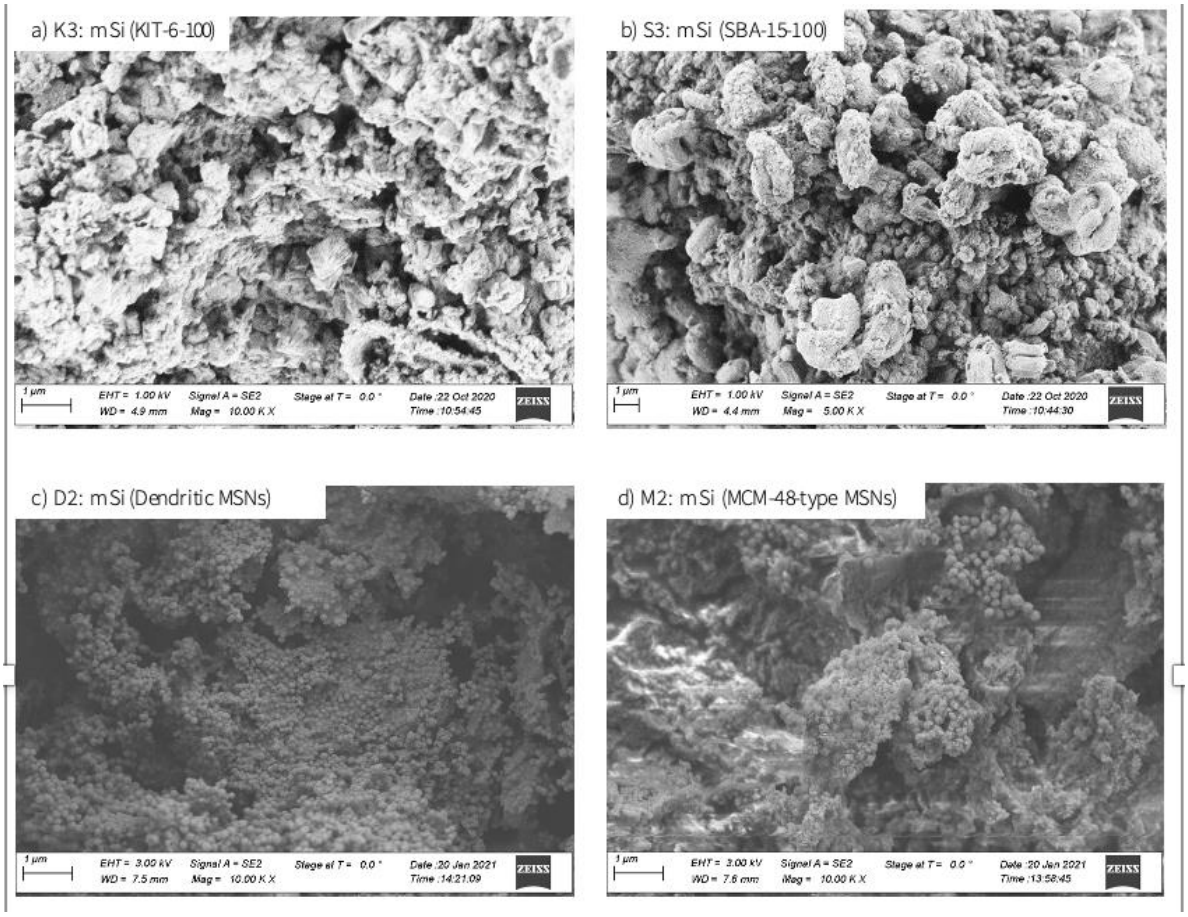

Figure 15: SEM images of the as-made mSi samples prepared from a) KIT-6, b) SBA-15 materials synthesised at 100°C, c) dendritic MSNs, and d) MCM-48-type MSNs synthesised via the adapted reduction protocol.

3.3.2 Composition Analysis

Similar to the composition of the mSi synthesised via traditional magnesiothermic reduction, almost pure silicon was obtained by adapting the etching protocol after reduction for samples obtained from the adapted reduction protocol (fig. 16). All results except for sample K3 contain peaks at $2\theta = 17°$, typical for the 001 reflection of $Mg(OH)_2$. 200 reflections from MgO at $2\theta = 43°$ are only present for the mSi product S3 made from SBA-15 aged at 100°C. S3 also shows small reflections from Mg_2Si at $2\theta = 40°$ and 53°, again resulting from slightly varying stoichiometry during magnesiothermic reduction. [125] [126]

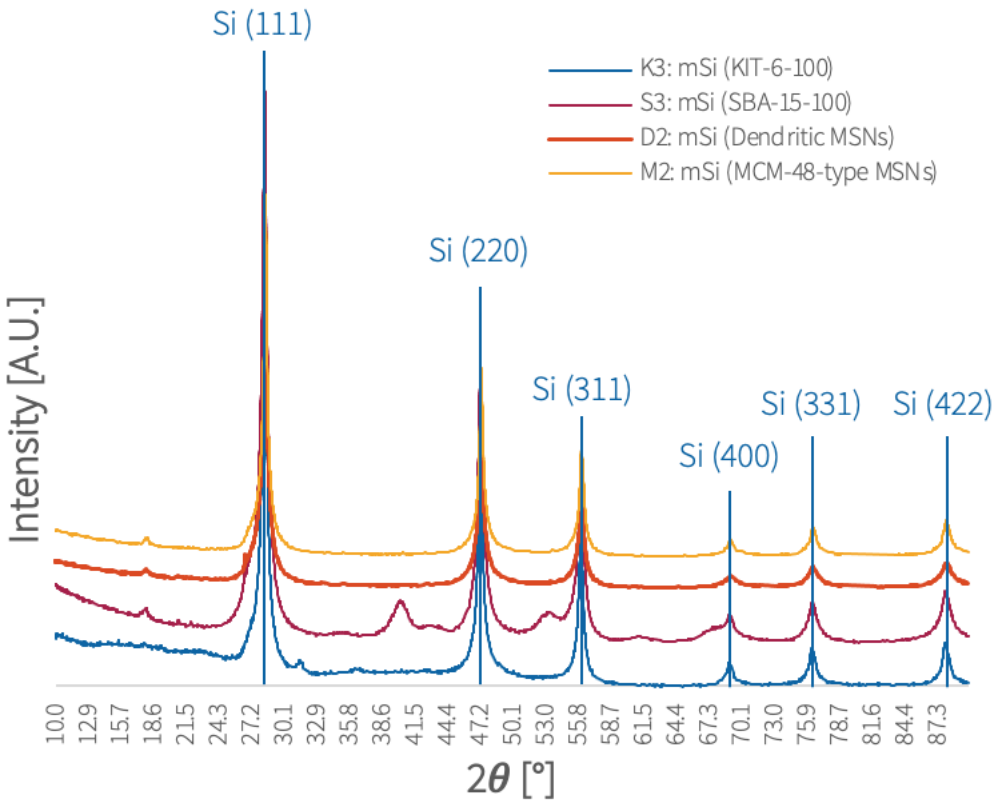

Figure 16: wide-angle XRD reflections of silicon samples synthesised with the NaCl heat scavenger during synthesis.

3.3.3 Electrochemical Analysis

The CCCV measurements of the adapted reduction protocol samples show similar results to the mSi products synthesised via the traditional magnesiothermic reduction method. The mSi from heat modulated reduction obtain specific charge values between 500 and 580 $mAh.g^{-1}$. Sample M2 made from MCM-48-type MSNs shows the highest initial specific capacity (580 $mAh.g^{-1}$), K3 made from KIT-6 has nearly the same specific charge values, ~570 $mAh.g^{-1}$. The highly porous structure of dendritic MSNs leads to lower specific charge of 550 $mAh.g^{-1}$. S3 has the lowest electrocatalytic activity with 500 $mAh.g^{-1}$.

Cycling stability for samples synthesised with both magnesiothermic reduction protocols is almost identical. The specific charge values of mSi obtained by heat modulated reduction are stable for the first 50 cycles, afterwards they decrease rapidly. After 80-90 cycles, total silicon material failure occurs for all materials.

3.4 Comparison of Samples analysed after different Posttreatments

3.4.1 Pore Structure and Surface Analysis

Further insights into the impact of HCl and HF as etching agents on the final materials' morphology properties and electrochemical performance needed to be made. Therefore, samples synthesised via heat modulator reduction routine are analysed after different etching progress.

In general, materials with both HCl and HF, and only HCl post-treatment possess similar SSAs. While samples with complete posttreatment have SSAs ranging from 99 to 177 m^2/g, samples only etched with HCl have SSAs between 147 and 167 m^2/g. SSAs between 60 and 99 m^2/g are achieved for untreated materials, since they contain high amounts MgO blocking the pores.

Mesopore volume results (0.12-0.72 cm^3/g) correlate to the SSAs of the mSi products. Samples which endured at least HCl treatment have much higher mesopore volumes (0.55-0.77 cm^3/g), while untreated samples contain MgO that lowers the available volume (0.12-0.28 cm^3/g). Thermal processes happening during the reduction lead to mode pore sizes ranging between 6 and 22 nm. For all samples except S3 and untreated samples mode pore size increases in comparison to the ordered silica material. An explanation is that void spaces are embedded inside the particles when they are exposed to great heat and sinter together. Sample S3 exhibits smaller mode pore size after reduction, which can be associated with pores partially closing due to melting as described before. Untreated samples all have smaller mode pore size, which fits under the assumption of MgO blocking the pores (table 6).

N_2 isotherms measured at 77K all show type IV(b) isotherms, typical for mesoporous materials with mesopores larger than 4 nm (fig. 17a-d). H3/H4 hybrid type hysteresis indicate that the original highly ordered porosity is lost. The adsorbed volume of N_2 at standard temperature and pressure (STP) confirms the effect pore blocking by MgO. Samples without post-treatment have much less accessible surface area (60-99 m^2/g) in comparison with partly and fully treated samples, which have similar SSAs (99-177 m^2/g) . The only exception is the fully post-treated sample S3, which has a SSA of177 m^2/g, but lower adsorbed volume. The sharp increase of adsorbed N_2 volume at relative pressures $p/p_0 = 1$ correlates with the presence of large interparticle voids inside/between the particles.

Table 6: Specific surface area, NLDFT pore volume up to 50 nm, and mode pore size of (partly) post treated silicon materials synthesised with a heat scavenger.

sample		etching treatment	BET-surface area [m²/g]	NLDFT pore volume up to 50 nm [cm³/g]	NLDFT mode pore size [nm]
mSi (KIT-6-100)	K3	HCl + HF	129	0.60	22.0
	K4	HCl	147	0.55	14.1
	K5	-	99	0.18	6.7
mSi (SBA-15-100)	S3	HCl + HF	177	0.41	4.9
	S4	HCl	153	0.72	18.5
	S5	-	64	0.12	6.3
mSi (Dendritic MSNs)	D2	HCl + HF	149	0.41	18.6
	D3	HCl	159	0.66	14.4
	D4	-	115	0.28	6.4
mSi (MCM-48-type-MSNs)	M2	HCl + HF	99	0.75	22.1
	M3	HCl	167	0.57	14.7
	M4	-	60	0.14	6.2

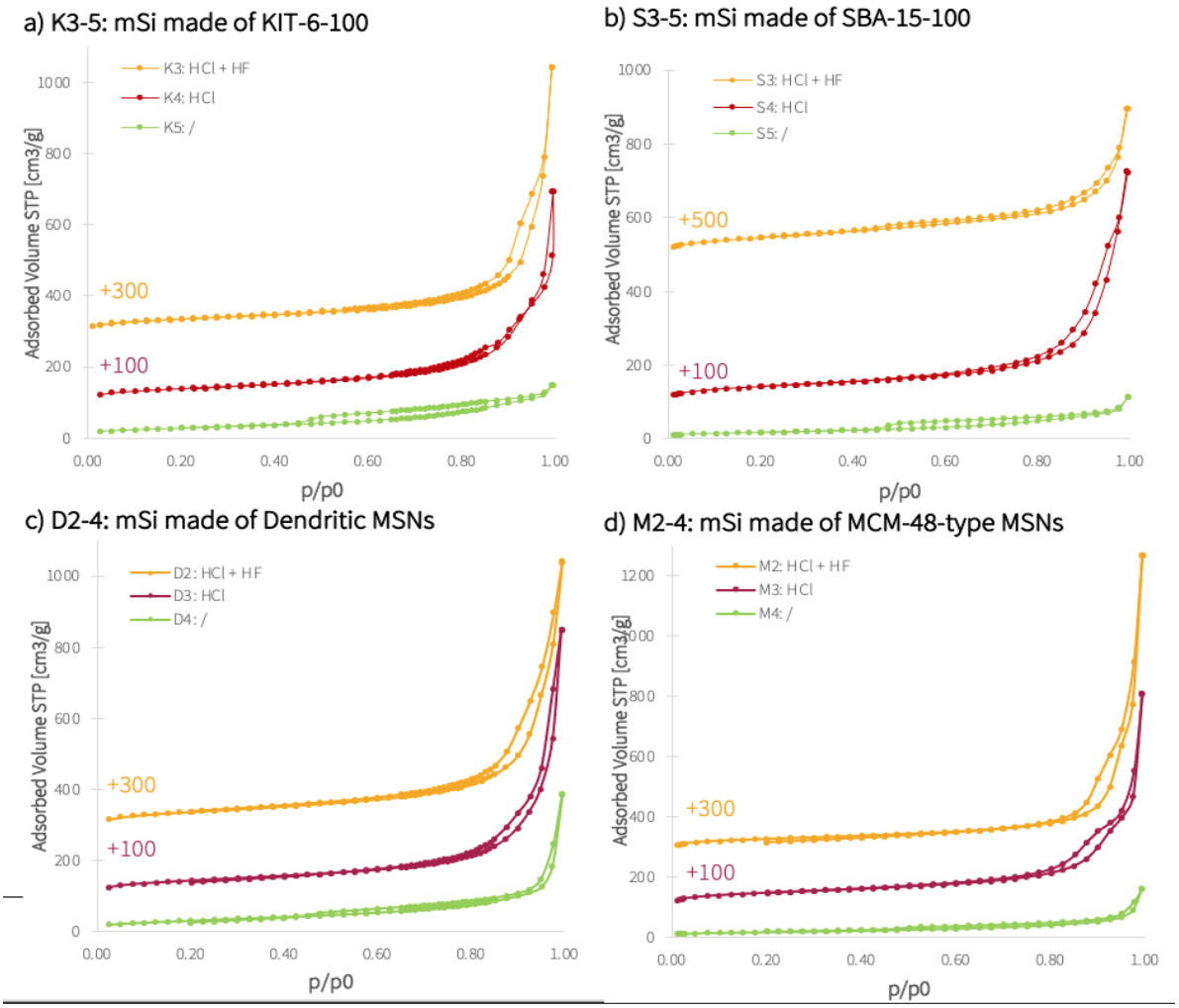

Figure 17: a-d) N_2 physisorption isotherms measured at 77 K for samples synthesised with the adapted NaCl heat scavenger reduction routine and analysed after different posttreatments.

The meso structure of the mSi samples is exposed by TEM imaging, to reveal the pore structure and particle shape of the materials after different etching posttreatment progress (fig. 18, 19). Despite the use of a heat modulator, all mSi materials have agglomerated into clusters of (nano-)particles. Materials which underwent both HCl and HF treatment have mesopores and enclosed void spaces between sintered particles. The shape of the original silica particle is still visible for all mSi samples made from dendritic and MCM-48-type MSN, whereby it can be seen best for samples D3 and M3 which had only HCl as the etching agent. This makes sense, since the HF procedure is very harsh and partly etches the mSi' surface features. For the samples without posttreatment, the pore features are hardly detectable due to the MgO distributed throughout the pores of the material. Void spaces formed during reduction also seem to be filled with impurities. Lower microscope magnifications give a better view of the extent of the effects of the sintering procedure for the nanoparticles. Dendritic as well as MCM-48-type MSNs images show accumulations of nanoparticles nearly retaining their original shape.

SEM images offer an overview of the materials surface structure after different etching procedures (fig. 20, 21). For partially treated and untreated samples, the surface features appear intact. In comparison, the damage from the HF etching is clearly observable on the surface of the fully treated samples. Images in the range of a few micrometres further show that the sintering affects large parts of the materials. The shape of the nanoparticles is still preserved, especially for samples without HF treatment. The HF etches the sintered agglomerates, resulting in the loss of the original particle shape. After the removal of MgO by HCl, the sintered nanoparticles are still clearly recognizable.

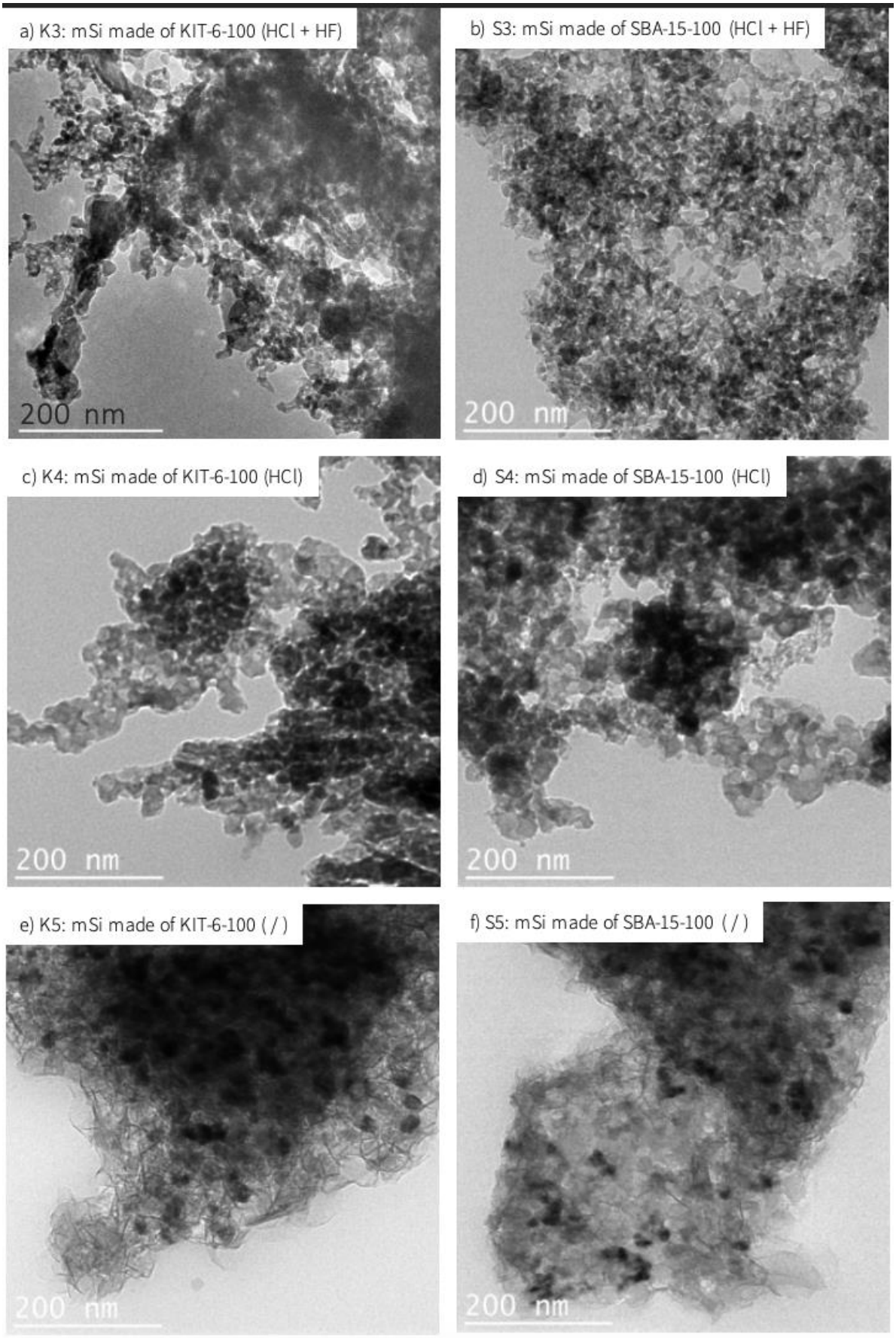

Figure 18: a-f) TEM images of mSi samples made from KIT-6 and SBA-15 bulk materials synthesised via magnesiothermic reduction with a heat scavenger and analysed after different posttreatments.

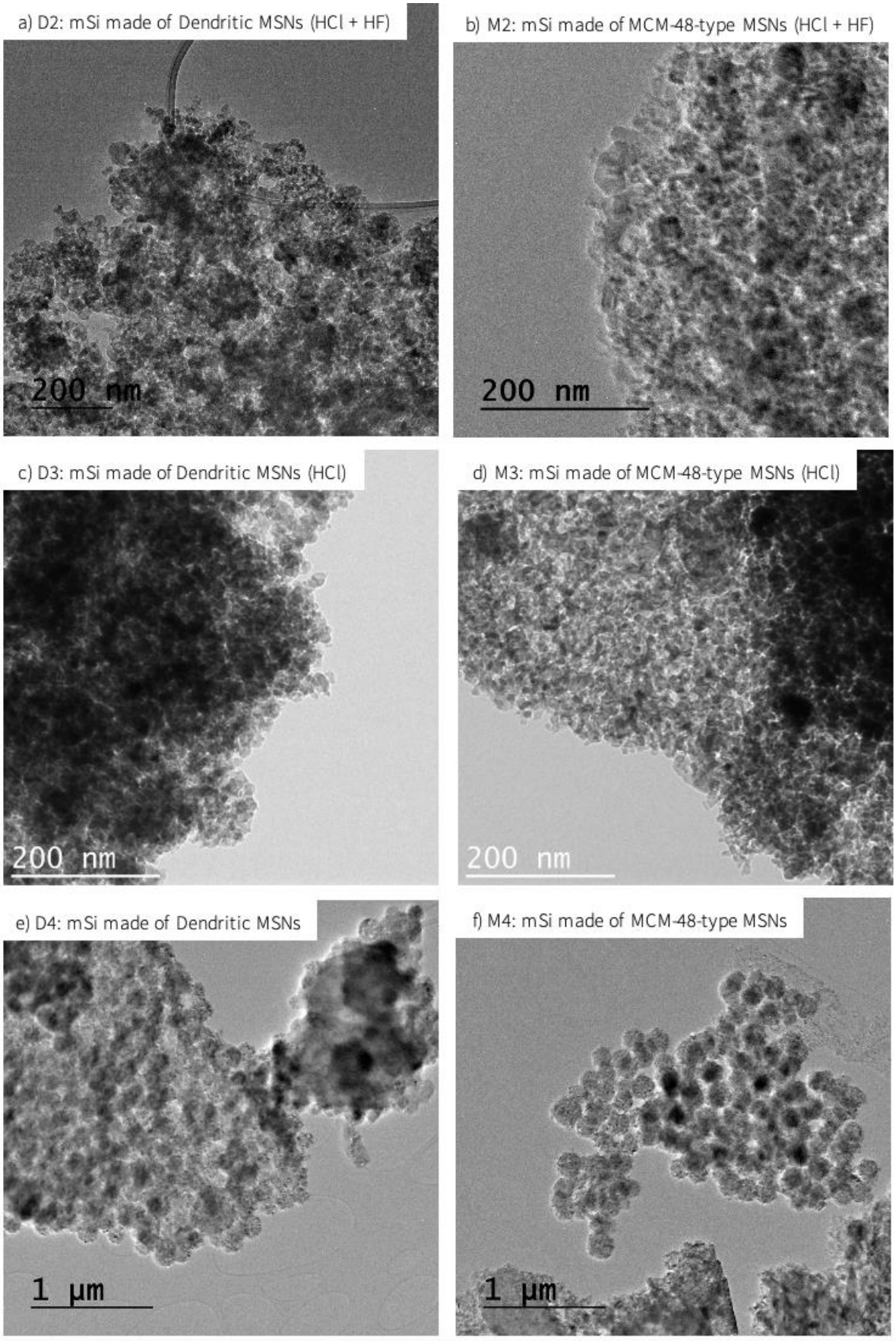

Figure 19: a-f) TEM images of mSi samples made from KIT-6 and SBA-15 bulk materials synthesised via magnesiothermic reduction with a heat scavenger and analysed after different posttreatments.

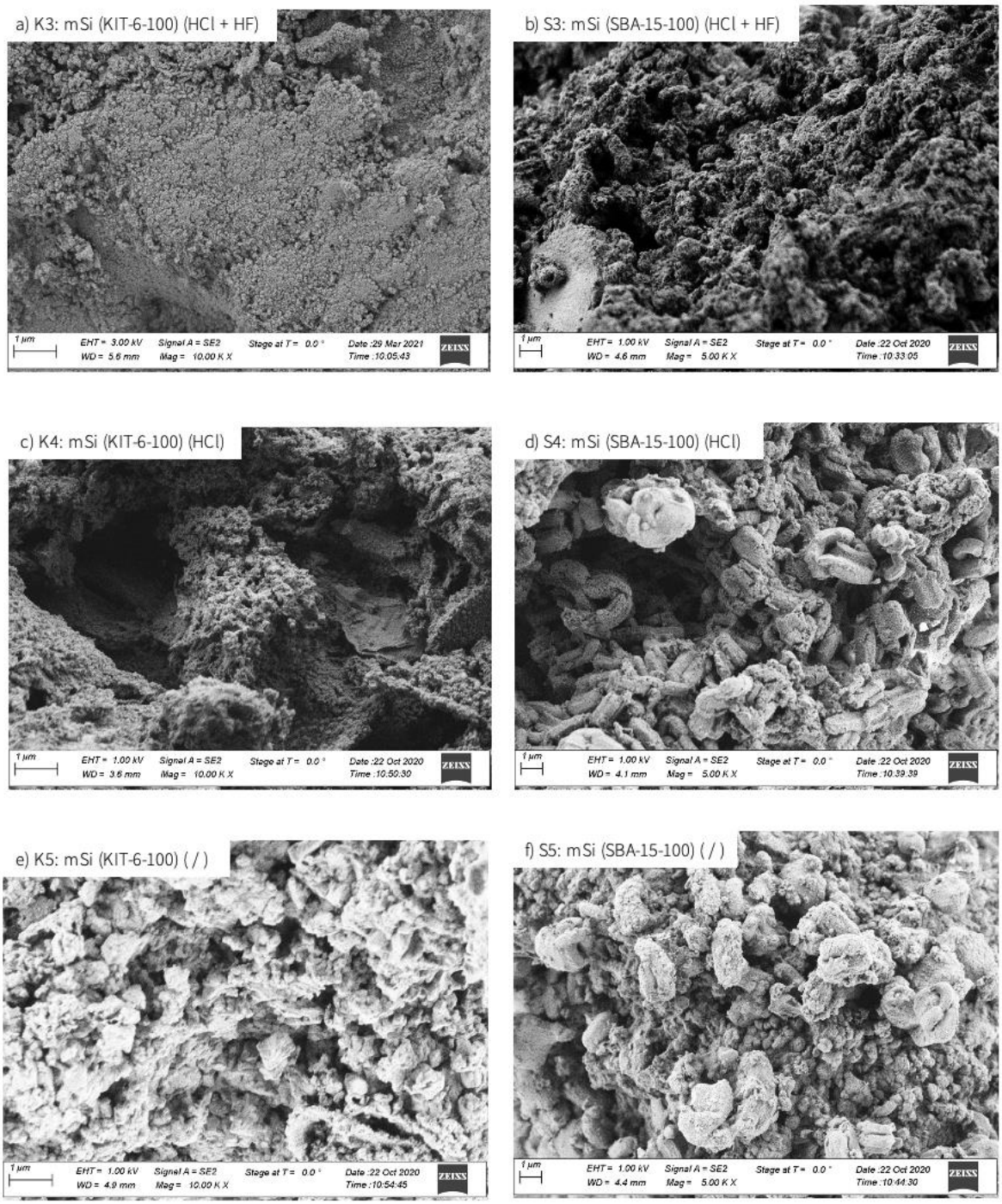

Figure 20: SEM images of as-made mSi samples prepared from KIT-6 and SBA-15 materials synthesised at 100°C: a,b) after etching with HCl and HF, c,d) after etching with HCl, and e,f) without posttreatment.

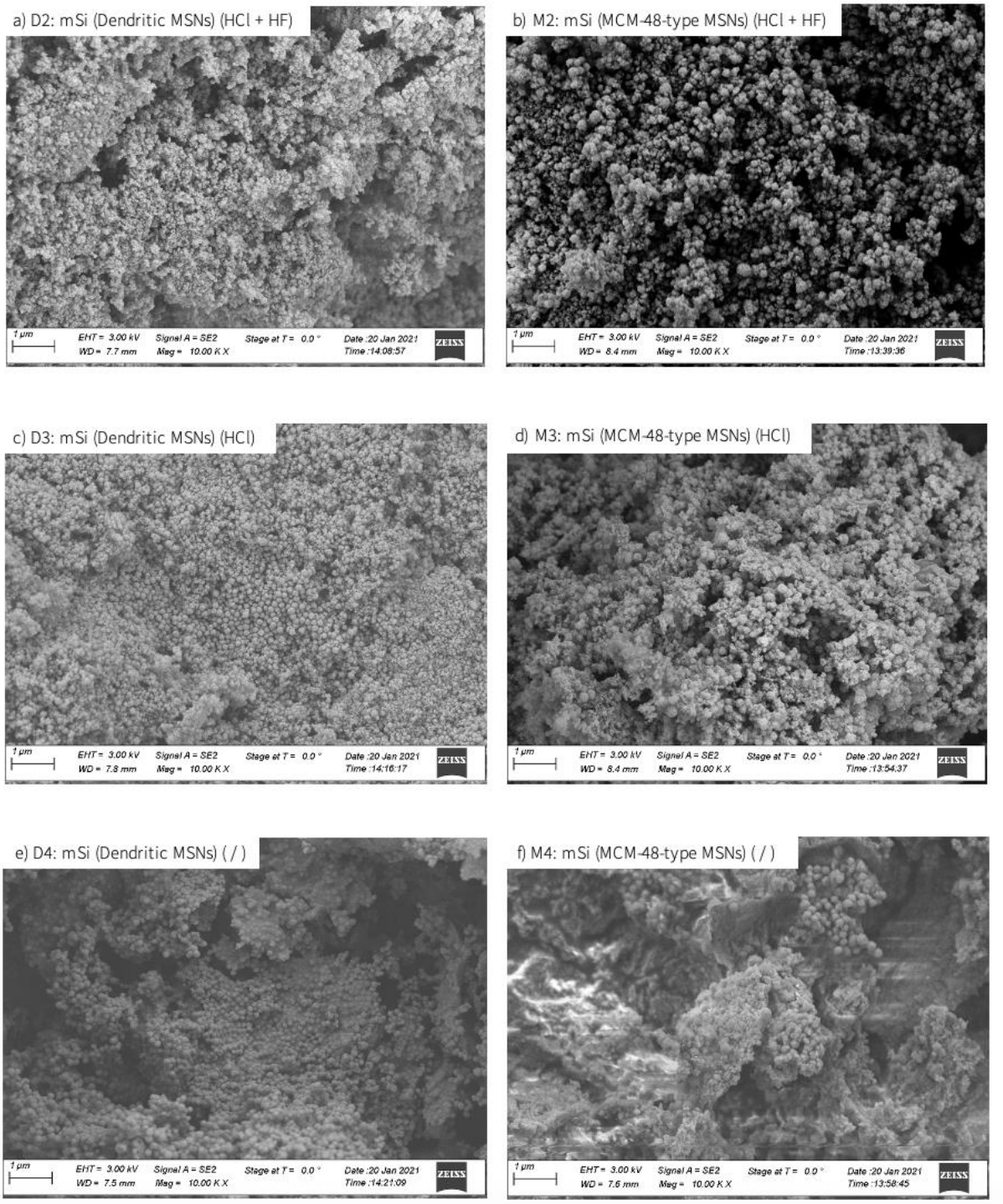

Figure 21: SEM images of as-made mSi samples prepared from MCM-48-type and dendritic MSNs nanomaterials a,b) after etching with HCl and HF, c,d) after etching with HCl, and e,f) without posttreatment.

3.4.2 Composition Analysis

The composition of samples and the identification of remaining impurities after incomplete etching treatment is revealed via XRD-studies. A new etching procedure, including an additional etching step, was included to improve purity. Fig. 22 shows all the XRD-reflections for the 4 different particle types.

The fully treated materials are nearly phase pure silicon. Only S3, made from SBA-15 aged at 100°C, shows reflections of Mg_2Si at 2θ = 40° and 53°.[127] [128] Traces of $Mg(OH)_2$ (2θ = 17°) are still present in some samples, but the amount is reduced in comparison with the amount present in samples synthesised via traditional magnesiothermic reduction.

The XRD reflections of samples without HF-treatment also seem to be almost phase pure, containing only small amounts of MgO. Products washed only with ethanol and H_2O, but without additional HCl or HF etching on the other hand still contain large amounts of MgO. Samples analysed without posttreatment show not only the strong 200 reflection at 2θ = 43°, but also 111 (37°), 220 (62°), 311 (74°) and 222 (78°) reflection peaks of MgO, respectively.

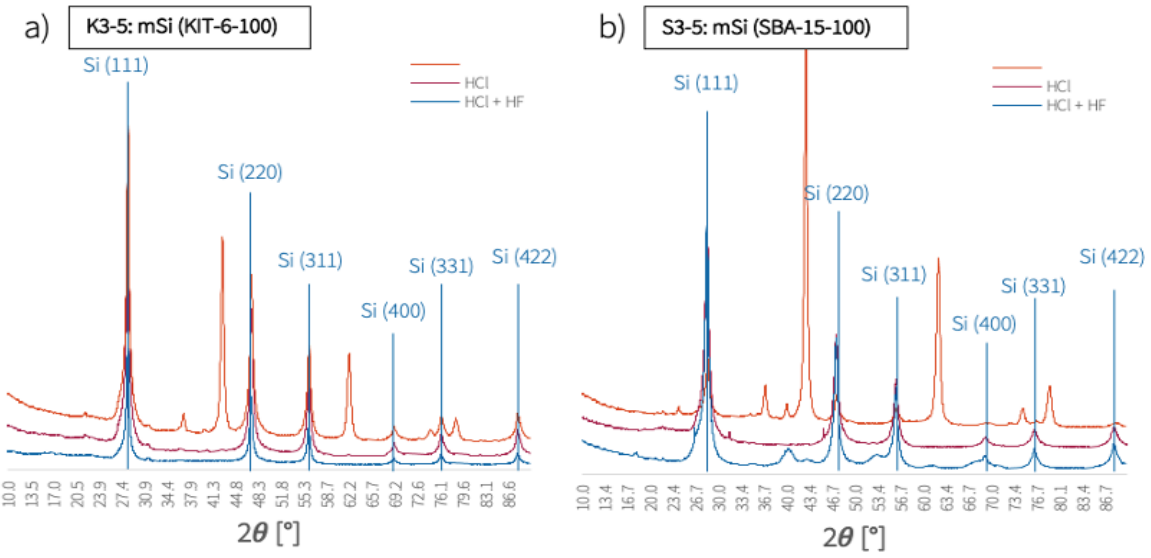

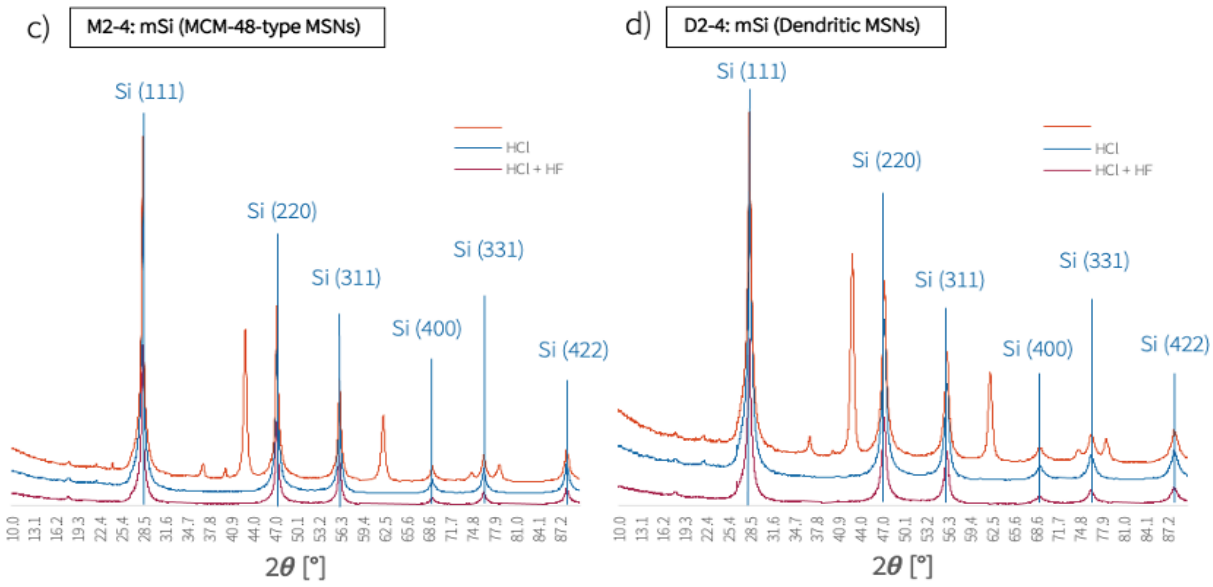

Figure 22: a-d) wide-angle XRD patterns of silicon samples synthesised with the adapted heat scavenger synthesis protocol and different etching posttreatment.

3.4.3 Electrochemical Analysis

The influence of impurities on the electrochemical cycling performance is investigated for mSi materials, which were synthesised with a heat scavenger and underwent different chemical post-treatments. Therefore, CCCV measurements at charging rates of 325 and 65 mA.g^{-1} (C/2 and C/10) are executed (fig. 23).

Directly after magnesiothermic reduction of OMS, products contain a large amount of MgO, and show hardly any electrochemical activity. Thus, the Si/C electrodes prepared from these samples show no increase in specific charge compared to pure graphite. After treatment with HCl, the electrochemical performance of mSi samples improves. Electrodes consisting of the pre-treated materials have a substantial increase in specific charge of ~100 mAh.g^{-1}. A further treatment with dilute HF additionally removes oxidized surface species. Electrodes prepared with fully treated bulk materials show good electrochemical properties and increases in specific charge values of up to 200 mAh.g^{-1}. Anodes containing MCM-48-type nanoparticles have slightly larger increases in specific charge (250 mAh.g^{-1}). The dendritic sponge-like pore structure doesn't seem to positively affect the material, with specific charge values in the range of SBA-15 and KIT-6 materials.

Materials analysed after both HCl and HF and only HCl etching show similar cycling stability. In general, after 50-70 cycles the specific charge value decreases rapidly. For some samples,

total electrode failure is reported after this many charging/discharging cycles. Samples without any post-treatment don't have this problem, since the synthesised material doesn't seem to have electrocatalytic activity. All materials analysed without the etching treatment still have stable specific charge values after 100 cycles.

Charging rates seem to have a negligible impact on the resulting cycling stability and specific charges of the electrodes. Overall, there is no real trend between charging rates and cycling performance observable. Composite anodes containing silicon from KIT-6 and dendritic MSNs have slightly higher specific charge values at lower charging rates (65 $mA.g^{-1}$ (C/10)), while anodes containing silicon from SBA-15 and MCM-48-type MSNs have higher specific charge at a charging rate of 325 $mA.g^{-1}$ (C/2).

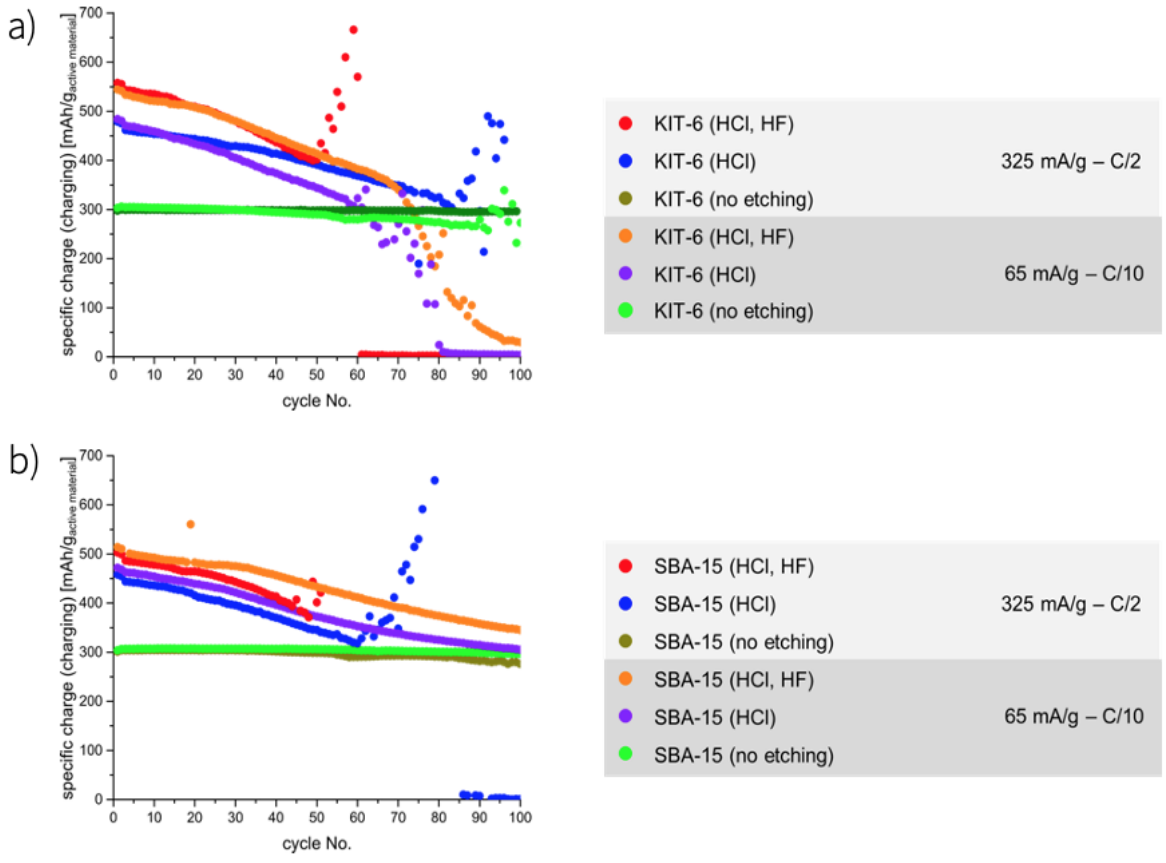

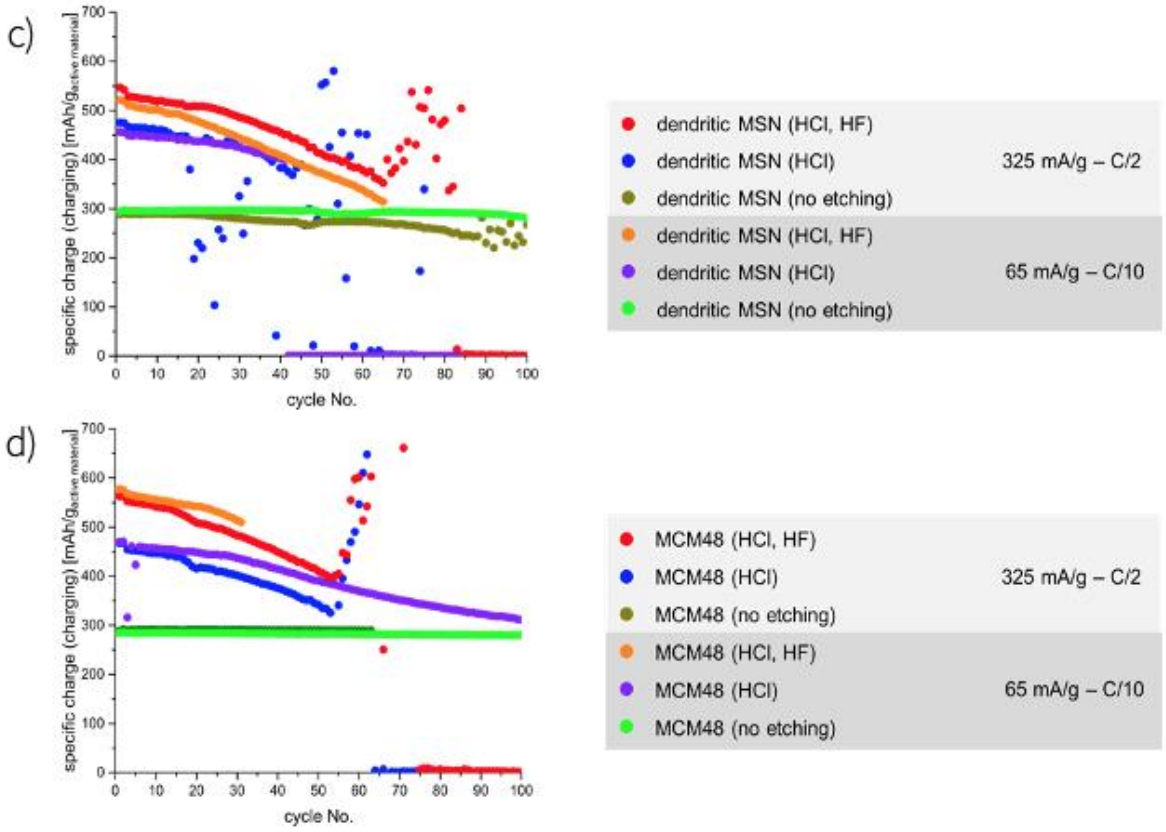

Figure 23: a-d) cycling performance for Si/C composite anodes. Mesoporous Si materials were synthesised via the heat scavenger reduction routine and post treated with HCl + HF, with only HCl, or without etching agent at all.

3.5 Structure and Composition Analysis of Prelithiated Samples

In order to achieve materials with better electrochemical cycling performance sample K3, prepared via adapted reduction protocol and fully etched with both HCl and HF afterwards, has further been used to test different prelithiation strategies. Wide-angle XRD patterns of the products offer more insights into the composition of the material. Identification of Li_xSi_x phases is critical since theoretical gravimetrical capacities alternate for different phases. Moreover, an overview of the phases that can be obtained with the chosen techniques is given. Only a small fraction of the total silicon is prelithiated, which leads to very small reflection peaks in comparison to the high intensity of the silicon patterns.

XRD results from the sample prelithiated using a hand milling routine, followed by a thermal treatment (L1a), doesn't show the desired patterns from new phases. The prelithiation in a suspension of silicon in cyclohexane and n-BuLi (L1b) and the mechanical impregnation of Li grains into the material (L1c), both under inert atmosphere deliver more promising results.

Both methods show reflection peaks at 2θ = 42° and 51°, an indicator of the existence of $Li_{15}Si_4$.[129] Unfortunately, 110 reflections at 2θ = 22°, as well as -202 (31°), 002 (32°), and -112 (35°) reflections confirm the formation of Li_2CO_3 on the surface of the material as well.[130]

The Li species formed via pre doping of Li are further investigated by SEM imaging of the prelithiated samples. New Li_xSi_y phases are indistinguishable on the silicon surface on images from all 3 procedures. A snowflake like structure is visible on some portions of the surface, especially for materials made using method b (fig. 25c). The structure is typical for Li_2CO_3, which was likely formed by the carbonization of Li during XRD-measurements under an atmosphere of air.

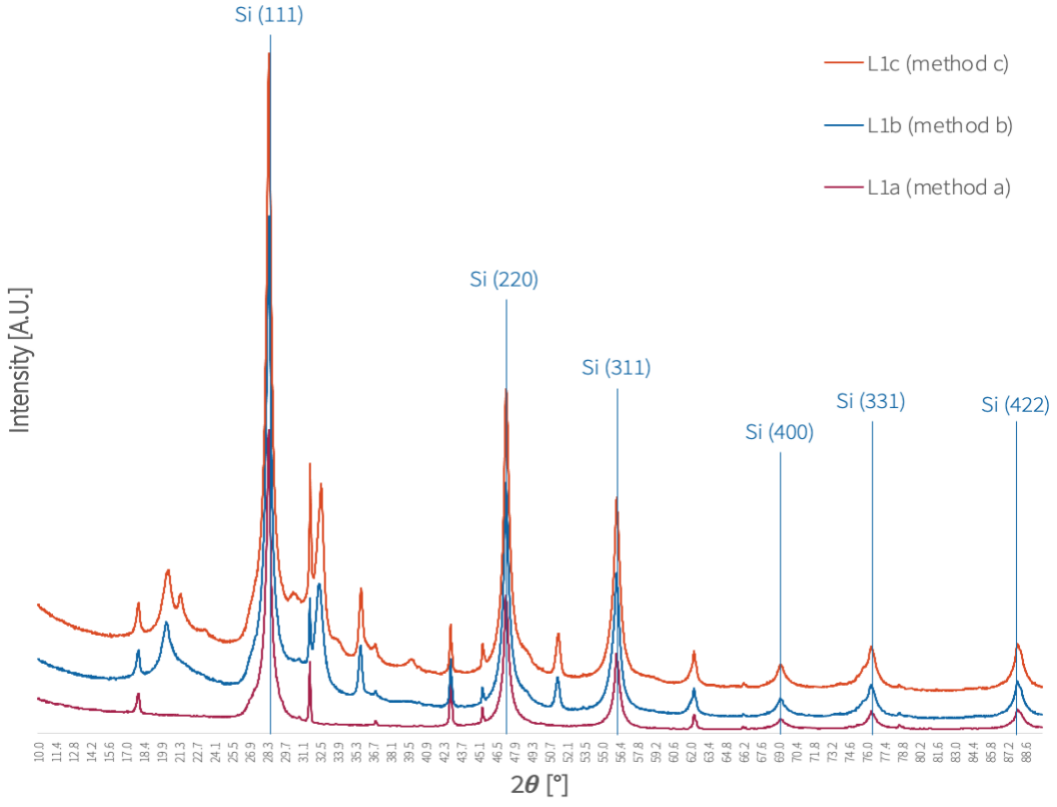

Figure 24: wide-angle XRD patterns of mSi samples made from K3 (KIT-6 synthesised at 100°C) after different prelithiation strategies.

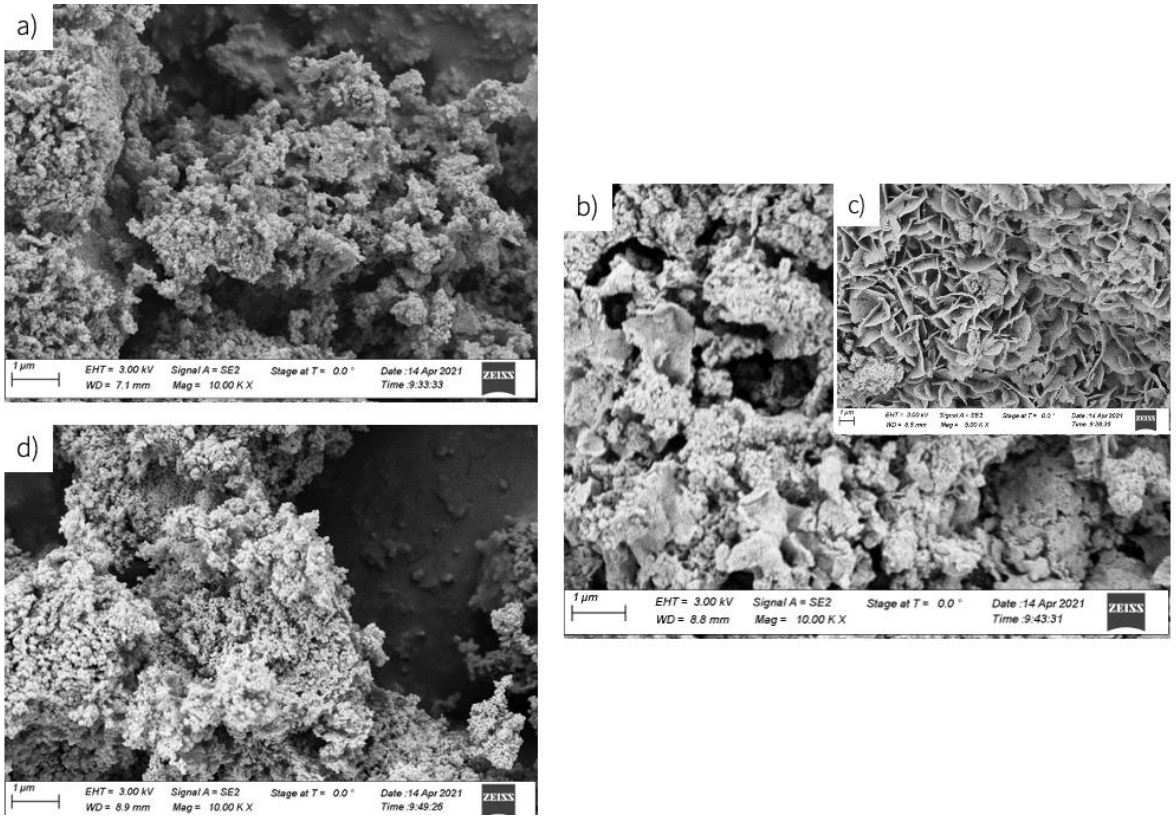

Figure 25a-d: SEM images of prelithiated mSi made from KIT-6-100. Prelithiation was conducted after 3 different synthesis procedures. Image a) method a, b) and c) method b, and d) method c.

The procedure used for sample L1b is also applied for mSi samples made from other silica sources. The mSi used for the prelithiation underwent complete posttreatment and partial posttreatment prior to XRD analysis (fig. 26). The results for the in total 8 samples look as expected from sample L1b. 110 reflections at $2\theta = 22°$, as well as -202 (31°), 002 (32°), and -112 (35°) reflections confirm the formation of Li_2CO_3. A peak at $2\theta = 51°$ may again result from $Li_{15}Si_4$, whereby the other significant reflection peak at 42° is missing.

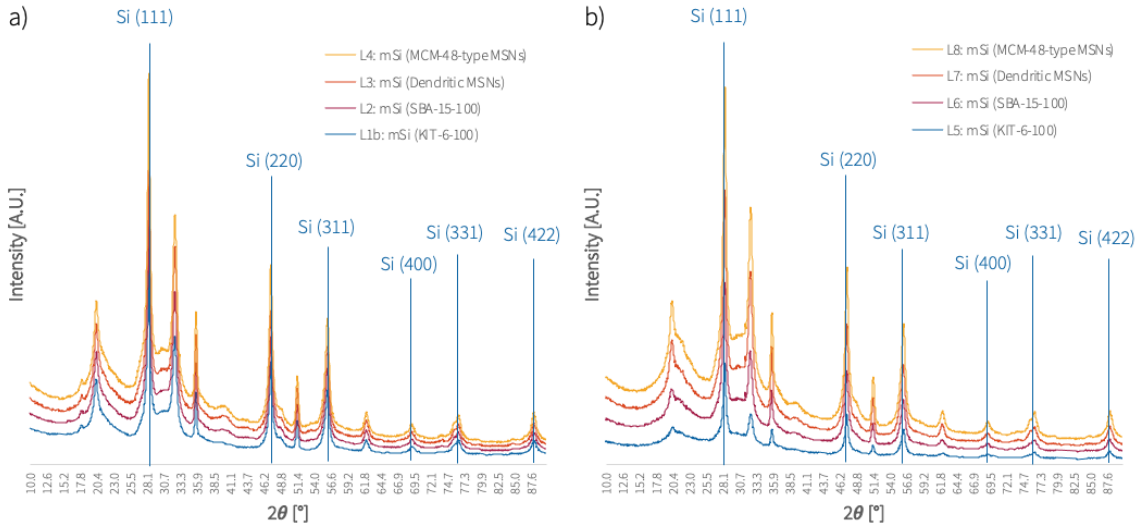

Figure 26: wide-angle XRD reflections of mSi samples after different prelithiation strategies. Samples underwent synthesis after a) full posttreatment (HCl + HF) and b) partial treatment (HCl).

4 Discussion

4.1 Physio-Chemical Properties

Physio-chemically properties and electrochemical cycling performance of four different OMS materials (KIT-6-100, SBA-15-100, MCM-48-type MSNs, and dendritic MSNs) are investigated in this study. The overall influence of pore geometry, pore size, and particle size of the four materials to achieve (ordered) mSi materials over magnesiothermic reduction is determined. Following a traditional reduction protocol, doesn't show much influence of the pore and particle parameters on the resulting silicon materials. The ordered mesoporous structure of the silica materials, as well as the mesopore size and/or shape, isn't preserved due to high heat release during the reduction. Nevertheless, the number of mesopores of the resulting silicon products and SSAs between 80 and 280 m^2/g are still promising for electrode materials. Actually, very high surface areas are not necessarily desirable for battery materials as they have a tendency to collapse faster under an electrochemical potential.

The results of samples prepared via adapted reduction protocol, including the use of a NaCl heat scavenger to absorb the heat released during the exothermic reduction step, show high similarities to the materials synthesised without heat modulation. SSAs between 100-180 m^2/g are in the desired range to use the mSi as electrode materials, similar to samples synthesised without an additional heat scavenger. Only the material made from SBA-15-100 has mode pore size comparable to the silica precursor material at 4.5 nm. In general, mSi prepared with a heat scavenger have larger mode pore sizes (~20 nm) than the products obtained from the traditional reduction. Except sample S3 made from SBA-15 aged at 100°C, which has mode pore size comparable to the silica precursor at 4.5 nm all mSi products all samples have pore size averages in this range. The enlargement of the pores makes it difficult to quantify the effects of the pore geometries of the starting materials. Despite the claims made in the literature, one may also question the efficiency of NaCl as a heat scavenger, since very few differences were obtained for the mesoporous samples made with and without NaCl in this work. Further work is needed to acquire more knowledge about the connection between the heat modulator and the in average larger pore size of samples prepared from this magnesiothermic reduction protocol.

The most critical parameter affecting the surface properties, appears to be the etching process. Indeed, materials made without post-treatment exhibited lower SSAs and mesopore volumes

due to pore blocking by high amounts of MgO by-products. Materials with both HCl and HF treatment show similar characteristics to those post treated with HCl only, which is expected since major by-products are magnesium-based oxides (MgO and $Mg(OH)_2$). Furthermore, wide-angle XRD analysis confirms that phase pure silicon (no Mg_2Si and Mg_2SiO_4) can be obtained without the laborious post-treatment with HF if the ratio of the reaction compounds is controlled precisely. The only downside for samples without HF etching is that the electrocatalytic cycling performance is lower, probably resulting from oxidized surface groups lowering the charging activity on the materials' surface.

Of all the materials synthesised via traditional or adapted magnesiothermic reduction, sample K1, obtained from KIT-6 synthesised at 100°C, delivers the most promising physio-chemical results. Although, SEM/TEM images (fig.8, 9) and the absence of the characteristic 3D body-centered cubic Ia3d space group reflections in low-angle XRD region (fig.7) confirm that the uniform pore size and highly ordered pore structure of the precursor material is lost, the high SSA (280 m^2/g) and pore volume (0.55 cm^3/g) indicates a high porosity for this sample (table 4). The porous features of this K1 sample are still among the highest ones reported so far for silicon materials. Even though pore number decreases due to thermal effects, the mesostructure is more porous than for silicon products synthesised with traditional routines. Also, the other samples generated in the framework of this project preserve a high number of pores and high SSAs (80 – 190 m^2/g) after reduction, which is a valuable characteristic for anode materials catalytic performance. It can be concluded that the combination of magnesiothermic reduction and OMS starting materials is a promising technique to obtain highly mesoporous silicon materials, which can also be used for further anode materials experiments or alternative applications.

4.2 Electrochemical Performance

All materials synthesised, with or without a heat modulator have almost equal cycling stability. Furthermore, the cycling performances of mSi materials prepared from the same OMS source are similar, with specific charge values between 450 and 580 $mAh.g^{-1}$ (fig.11, 23).
Coulombic efficiency after the 1st charging cycle is higher for commonly available silicon nanoparticles than for the mSi alternatives. Nanoparticles benefit from their higher stability during alloying with lithium due to their small size. Synthesised materials have a higher loss

of coulombic efficiency after the 1st charging cycle. Most likely the larger particle aggregates sintered together during reduction under high temperatures, negatively affect the performance. Another important aspect of electrocatalytic cycling measurements is that higher porosity is always related to higher SSA, which leads to enhanced SEI formation. The SEI unavoidably lowers electrocatalytic activity by consuming the active anode material.

Samples made from MCM-48-type MSNs, achieve the highest specific charges of all prepared samples. Specific charge values of 580 $mAh.g^{-1}$ and 1st coulombic cycle efficiency of 79% clearly outperform purchasable bulk nanoparticles of similar size (130 nm). Only very small nanoparticles (30-50 nm) have higher specific charge values (> 600 $mAh.g^{-1}$). Normally, smaller nanoparticles also have much higher SSA, which should lead to enhanced SEI formation. It seems by decreasing nanoparticles size, the cracking resistance is even higher. This effect is significant enough to compensate the additional active electrode material loss, due to increased SEI formation with the electrolyte for samples with higher SSAs.

Unfortunately, the porous material alternatives cannot keep up with common available in terms of endurance and cycling stability. The results of the purchasable nanoSi still shows almost stable specific charge values after 100 cycles. For all mesoporous alternatives, full electrode failure occurs after 80-90 cycles. Specific charge values are dropping even earlier for some materials, after around 50 cycles.

4.3 Prelithiation Studies

New phases are reported for all materials prelithiated following one of the three pre-doping strategies (fig.24). Unfortunately, due to the high silicon content of the samples, the XRD-patterns of silicon appear very prominent in the results, whereby those of the small amounts of Li_xSi_y formed species are hardly detectable. Using the hand milling routine, followed by thermal treatment (L1a) for prelithiation, only gives insufficient reflection peaks originating from new phases and therefore isn't used for further samples. The other two options, prelithiation in a suspension of silicon in cyclohexane and n-BuLi (L1b) and the mechanical impregnation of Li grains into the material (L1c), both under inert atmosphere show more promising results. New reflection peaks indicate the existence of $Li_{22}Si_5$ and/or $Li_{15}Si_4$, the two phases with the highest theoretical capacity of all Li_xSi_y species. SEM images can't confirm the existence of $Li_{22}Si_5$ or $Li_{15}Si_4$, because undesired Li_2CO_3 is formed by carbonization of the Li after synthesis and covers the silicon surface. SEM images show the typical snow-flake

structure (fig.25). To clearly define the phases synthesised with this method, a stoichiometrically higher amount of Li and XRD analysis under inert atmosphere would be advantageous.

5 Conclusion

Surface and pore properties as well as electrocatalytic cycling performance of various mSi materials prepared via magnesiothermic reduction are investigated. OMS with different pore morphologies are used as starting materials. Several problems with the reduction emerged, including the aggregation of particles and the loss of ordered pore structure, due to heat accumulation. A new method that uses NaCl as a heat scavenger is applied for the reduction of OMS to avoid thermal effects. Nevertheless, the material with the most favourable physio-chemical characteristics is obtained from the synthesis without a heat modulator. mSi sample K1 made from KIT-6 aged at 100°C has a high porosity and SSA of 280 m^2/g. The high surface accessibility in combination with a specific charge value of 550 $mAh.g^{-1}$ relatively stable for 70 cycles, makes the mSi material a serious competitor to the available nanoparticles tested. Nanoparticles made from MCM-48-type MSNs (M1, M2) have even higher specific charge values (580 $mAh.g^{-1}$) than bulk materials (KIT-6, SBA-15) during cycling tests, likely due to the higher stress resistance of nanosized particles. Both materials (M1, M2) outperform specific charge values (for ~70 cycles) and 1st cycle coulombic efficiencies achieved by widely available nanoSi (130 nm). Only smaller nanoSi (30-50 nm) can surpass the electrocatalytic cycling properties of the mSi alternatives.

The primary target of the work is to determine the effect of pore structure, pore size and particle size on the performance of the resulting mSi material. Smaller particle sizes under a critical threshold (~150 nm) seem to allow the material to endure more stress during cycling. Different pore sizes and pore structures don't show any clear effects. The thermal effects are approximately equivalent equal, whether it be 2-, 3-dimensional or sponge-like pore networks. Nevertheless, mesoporous silicon materials can be made by magnesiothermic reduction of OMS starting materials with or without heat modulation.

Generally, the synthesis of silicon with a NaCl heat scavenger remains questionable. The products of both methods are sintered together and suffer a loss of ordered porosity, which suggests that the thermal effects can't be mitigated by the addition of NaCl. Additional studies are required to better understand the methodology of heat modulation and to also implement magnesiothermic reduction on larger scales, which remains a big problem due to inhomogeneous heat excess. The experimental setup could be one explanation for an uneven

heat distribution, since the sample's surface where the reduction takes place, is not equally exposed in the crucible under linear gas flow.

The exact role of each etching step on the physio-chemical and electrochemical properties of the resulting mSi material is also determined. The experiments demonstrate that phase pure silicon samples can still be obtained without HF processing, if the stoichiometry for the reaction is precisely controlled. An interesting new aspect since working with HF generally is laborious and very dangerous. Furthermore, physio-chemical properties like SSA and average pore sizes are similar to them of fully treated materials. Only the electrochemical properties decrease due to the formation of inactive oxidized surface groups (-OH groups).

Another technique which should improve electrochemical cycling performance of the mSi electrode materials is prelithiation. Two of the applied methods, lead to the formation of interesting Li_xSi_y phases with high specific capacities (3579 or 4200 $mAh.g^{-1}$). Nevertheless, two problems appear during the process. The newly formed phases are difficult to analyse, since only a small percentage of the silicon samples is prelithiated and Li_2CO_3 formed by carbonization after synthesis covers the mSi' surface. A higher ratio of Li source for prelithiation and working under inert atmosphere during materials characterisation could ease the problems for future experiments.

The findings of this master's thesis project provide clearer understanding of the fabrication of high-capacity silicon electrode materials using magnesiothermic reduction with OMS or also other silica sources as starting materials. The reduction method furthermore offers a way to synthesise highly porous phase-pure silicon materials with pore sizes in the mesopore range without the dangerous HF processing. The obtained mSi materials are promising candidates for further attempts to achieve the next generation of silicon anode materials.

References

[1] European Commission, 2017, Energy Storage - The role of electricity SWD (2017) 61 final, European Commission, Brussels, pp: 1-25.

[2] S. Simons, J. Schmitt, B. Tom, H. Bao, B. Pettinato, and M. Pechulis, 'Advanced concepts', in *Thermal, Mechanical, and Hybrid Chemical Energy Storage Systems*, Elsevier, 2021, pp. 569–596

[3] S. Ould Amrouche, D. Rekioua, T. Rekioua, and S. Bacha, 'Overview of energy storage in renewable energy systems', *International Journal of Hydrogen Energy*, vol. 41, no. 45, pp. 20914–20927, Dec. 2016

[4] S. K. Biradar, R. A. Patil, and M. Ullegaddi, 'Energy storage system in electric vehicle', in *Power Quality '98*, Hyderabad, India, 1998, pp. 247–255,

[5] X. Zeng *et al.*, 'Commercialization of Lithium Battery Technologies for Electric Vehicles', *Adv. Energy Mater.*, vol. 9, no. 27, p. 1900161

[6] I. Gunnarsdottir, B. Davidsdottir, E. Worrell, and S. Sigurgeirsdottir, 'Sustainable energy development: History of the concept and emerging themes', *Renewable and Sustainable Energy Reviews*, vol. 141, p. 110770, May 2021

[7] J. Zhao *et al.*, 'Artificial Solid Electrolyte Interphase-Protected Li x Si Nanoparticles: An Efficient and Stable Prelithiation Reagent for Lithium-Ion Batteries', *Journal of the American Chemical Society*, vol. 137, Jun. 2015

[8] D. Ma, Z. Cao, and A. Hu, 'Si-Based Anode Materials for Li-Ion Batteries: A Mini Review', *Nano-Micro Lett.*, vol. 6, no. 4, pp. 347–358, Oct. 2014

[9] Z. Liu *et al.*, 'In-Situ Crosslinked PVA-PEI Polymer Binder for Long-Cycle Silicon Anodes in Li-ion Batteries', *RSC Adv.*, vol. 6, Jan. 2016

[10] M. Oswal, J. Paul and R. Zhao, "A comparative study of lithium-ion batteries", 2010.

[11] N. Nitta, F. Wu, J. T. Lee, and G. Yushin, 'Li-ion battery materials: present and future', *Materials Today*, vol. 18, no. 5, pp. 252–264

[12] Goonan, T.G., 2012, Lithium use in batteries: U.S. Geological Survey Circular 1371, 14 p.

[13] C. Iclodean, B. Varga, N. Burnete, D. Cimerdean, and B. Jurchiş, 'Comparison of Different Battery Types for Electric Vehicles', *IOP Conf. Ser.: Mater. Sci. Eng.*, vol. 252, p. 012058

[14] X. Shen *et al.*, 'Advanced Electrode Materials in Lithium Batteries: Retrospect and Prospect', *Energy Material Advances*, vol. 2021, Jan. 2021

[15] H. Li, 'Practical Evaluation of Li-Ion Batteries', *Joule*, vol. 3, no. 4, pp. 911–914, Apr. 2019

[16] J. Asenbauer, T. Eisenmann, M. Kuenzel, A. Kazzazi, Z. Chen, and D. Bresser, 'The success story of graphite as a lithium-ion anode material – fundamentals, remaining

challenges, and recent developments including silicon (oxide) composites', *Sustainable Energy Fuels*, vol. 4, no. 11, pp. 5387–5416, 2020

[17] D. Andre, H. Hain, P. Lamp, F. Maglia, and B. Stiaszny, 'Future high-energy density anode materials from an automotive application perspective', *J. Mater. Chem. A*, vol. 5, no. 33, pp. 17174–17198, Aug. 2017

[18] L. Lavagna, G. Meligrana, C. Gerbaldi, A. Tagliaferro, and M. Bartoli, 'Graphene and Lithium-Based Battery Electrodes: A Review of Recent Literature', *Energies*, vol. 13, no. 18, p. 4867, Sep. 2020

[19] S. Hossain, Y.-K. Kim, Y. Saleh, and R. Loutfy, 'Comparative studies of MCMB and C□C composite as anodes for lithium-ion battery systems', *Journal of Power Sources*, vol. 114, no. 2, pp. 264–276, Mar. 2003

[20] S. Goriparti, E. Miele, F. De Angelis, E. Di Fabrizio, R. Proietti Zaccaria, and C. Capiglia, 'Review on recent progress of nanostructured anode materials for Li-ion batteries', *Journal of Power Sources*, vol. 257, pp. 421–443

[21] B. Scrosati and J. Garche, 'Lithium batteries: Status, prospects and future', *Journal of Power Sources*, vol. 195, no. 9, pp. 2419–2430

[22] B. J. Landi, M. J. Ganter, C. D. Cress, R. A. DiLeo, and R. P. Raffaelle, 'Carbon nanotubes for lithium ion batteries', *Energy Environ. Sci.*, vol. 2, no. 6, p. 638, 2009

[23] J. Hou, Y. Shao, M. W. Ellis, R. B. Moore, and B. Yi, 'Graphene-based electrochemical energy conversion and storage: fuel cells, supercapacitors and lithium ion batteries', *Phys. Chem. Chem. Phys.*, vol. 13, no. 34, p. 15384, 2011

[24] J. Yang, 'SiOx-based anodes for secondary lithium batteries', *Solid State Ionics*, vol. 152–153, pp. 125–129, Dec. 2002

[25] I.-S. Hwang, J.-C. Kim, S.-D. Seo, S. Lee, J.-H. Lee, and D.-W. Kim, 'A binder-free Ge-nanoparticle anode assembled on multiwalled carbon nanotube networks for Li-ion batteries', *Chem. Commun.*, vol. 48, no. 56, p. 7061, 2012

[26] K. Zhuo, M.-G. Jeong, and C.-H. Chung, 'Highly porous dendritic Ni–Sn anodes for lithium-ion batteries', *Journal of Power Sources*, vol. 244, pp. 601–605, Dec. 2013

[27] J. Jiang, Y. Li, J. Liu, X. Huang, C. Yuan, and X. W. D. Lou, 'Recent Advances in Metal Oxide-based Electrode Architecture Design for Electrochemical Energy Storage', *Adv. Mater.*, vol. 24, no. 38, pp. 5166–5180, Oct. 2012

[28] Z. Wang, L. Zhou, and X. W. David Lou, 'Metal Oxide Hollow Nanostructures for Lithium-ion Batteries', *Adv. Mater.*, vol. 24, no. 14, pp. 1903–1911, Apr. 2012

[29] P. P. Prosini, M. Carewska, S. Loreti, C. Minarini, and S. Passerini, 'Lithium iron oxide as alternative anode for li-ion batteries', *International Journal of Inorganic Materials*, vol. 2, no. 4, pp. 365–370, Sep. 2000

[30] C.-T. Lin, T.-Y. Huang, J.-J. Huang, N.-L. Wu, and M. Leung, 'Multifunctional co-poly(amic acid): A new binder for Si-based micro-composite anode of lithium-ion battery', *Journal of Power Sources*, vol. 330, pp. 246–252, Oct. 2016

[31] A. Franco Gonzalez, N.-H. Yang, and R.-S. Liu, 'Silicon Anode Design for Lithium-Ion Batteries: Progress and Perspectives', *J. Phys. Chem. C*, vol. 121, no. 50, pp. 27775–27787, Dec. 2017

[32] M. N. Obrovac and L. Christensen, 'Structural Changes in Silicon Anodes during Lithium Insertion/Extraction', *Electrochem. Solid-State Lett.*, vol. 7, no. 5, p. A93, Mar. 2004

[33] X. H. Liu and J. Y. Huang, 'In situ TEM electrochemistry of anode materials in lithium ion batteries', *Energy Environ. Sci.*, vol. 4, no. 10, p. 3844

[34] A. Franco Gonzalez, N.-H. Yang, and R.-S. Liu, 'Silicon Anode Design for Lithium-Ion Batteries: Progress and Perspectives', J. Phys. Chem. C, vol. 121, no. 50, pp. 27775–27787, Dec. 2017

[35] J. Song *et al.,* 'Interpenetrated Gel Polymer Binder for High-Performance Silicon Anodes in Lithium-Ion Batteries', Advanced Functional Materials, vol. 24, Oct. 2014

[36] I. Kovalenko *et al.*, 'A Major Constituent of Brown Algae for Use in High-Capacity Li-Ion Batteries', *Science*, vol. 334, no. 6052, pp. 75–79, Oct. 2011

[37] H. Kim, M. Seo, M.-H. Park, and J. Cho, 'A Critical Size of Silicon Nano-Anodes for Lithium Rechargeable Batteries', *Angew. Chem. Int. Ed.*, vol. 49, no. 12, pp. 2146–2149, Mar. 2010

[38] H. Jia, P. Gao, J. Yang, J. Wang, Y. Nuli, and Z. Yang, 'Novel Three-Dimensional Mesoporous Silicon for High Power Lithium-Ion Battery Anode Material', *Adv. Energy Mater.*, vol. 1, no. 6, pp. 1036–1039, Nov. 2011

[39] R. A. Huggins and W. D. Nix, 'Decrepitation model for capacity loss during cycling of alloys in rechargeable electrochemical systems', *Ionics*, vol. 6, no. 1–2, pp. 57–63, Jan. 2000

[40] J. Yang, 'Small particle size multiphase Li-alloy anodes for lithium-ionbatteries', *Solid State Ionics*, vol. 90, no. 1–4, pp. 281–287, Sep. 1996

[41] H. Tian, F. Xin, X. Wang, W. He, and W. Han, 'High capacity group-IV elements (Si, Ge, Sn) based anodes for lithium-ion batteries', *Journal of Materiomics*, vol. 1, no. 3, pp. 153–169

[42] C. S. Wang, G. T. Wu, X. B. Zhang, Z. F. Qi, and W. Z. Li, 'Lithium Insertion in Carbon-Silicon Composite Materials Produced by Mechanical Milling', *J. Electrochem. Soc.*, vol. 145, no. 8, pp. 2751–2758

[43] X. H. Liu, L. Zhong, S. Huang, S. X. Mao, T. Zhu, and J. Y. Huang, 'Size-Dependent Fracture of Silicon Nanoparticles During Lithiation', *ACS Nano*, vol. 6, no. 2, pp. 1522–1531

[44] M. T. McDowell *et al.*, 'In Situ TEM of Two-Phase Lithiation of Amorphous Silicon Nanospheres', *Nano Lett.*, vol. 13, no. 2, pp. 758–764

[45] H. Ma *et al.*, 'Nest-like Silicon Nanospheres for High-Capacity Lithium Storage', *Adv. Mater.*, vol. 19, no. 22, pp. 4067–4070, Nov. 2007

[46] L.-F. Cui, R. Ruffo, C. K. Chan, H. Peng, and Y. Cui, 'Crystalline-Amorphous Core−Shell Silicon Nanowires for High Capacity and High Current Battery Electrodes', *Nano Lett.*, vol. 9, no. 1, pp. 491–495, Jan. 2009

[47] M.-H. Park *et al.*, 'Silicon Nanotube Battery Anodes', *Nano Lett.*, vol. 9, no. 11, pp. 3844–3847, Nov. 2009

[48] J. Wang, J. Yang, and S. Lu, 'A Mini Review: Nanostructured Silicon-based Materials for Lithium Ion Battery', *NANOASIA*, vol. 6, no. 1, pp. 3–27, Mar. 2016

[49] W. Qi, J. G. Shapter, Q. Wu, T. Yin, G. Gao, and D. Cui, 'Nanostructured anode materials for lithium-ion batteries: principle, recent progress and future perspectives', *J. Mater. Chem. A*, vol. 5, no. 37, pp. 19521–19540, Sep. 2017.

[50] Y. Yao *et al.*, 'Interconnected Silicon Hollow Nanospheres for Lithium-Ion Battery Anodes with Long Cycle Life', *Nano Lett.*, vol. 11, no. 7, pp. 2949–2954

[51] X. Li *et al.*, 'Mesoporous silicon sponge as an anti-pulverization structure for high-performance lithium-ion battery anodes', *Nat Commun*, vol. 5, no. 1, p. 4105

[52] I. S. Curtis, R. J. Wills, M. Dasog, 'Photocatalytic hydrogen generation using mesoporous silicon nanoparticles: influence of magnesiothermic reduction conditions and nanoparticle aging on the catalytic activity', Nanoscale, 2021, 13, 2685.

[53] Z. Bao *et al.*, 'Chemical reduction of three-dimensional silica micro-assemblies into microporous silicon replicas', *Nature*, vol. 446, no. 7132, pp. 172–175, Mar. 2007

[54] A. Darghouth, S. Aouida, and B. Bessais, 'High Purity Porous Silicon Powder Synthesis by Magnesiothermic Reduction of Tunisian Silica Sand', *Silicon*, Apr. 2020

[55] Y. Shen, 'Rice Husk Silica-Derived Nanomaterials for Battery Applications: A Literature Review', *J. Agric. Food Chem.*, vol. 65, no. 5, pp. 995–1004, Feb. 2017

[56] M. Ashuri, Q. He, and L. L. Shaw, 'Silicon as a potential anode material for Li-ion batteries: where size, geometry and structure matter', Nanoscale, vol. 8, no. 1, pp. 74–103, Dec. 2015

[57] J. Entwistle, A. Rennie, and S. Patwardhan, 'A review of magnesiothermic reduction of silica to porous silicon for lithium-ion battery applications and beyond', *J. Mater. Chem. A*, vol. 6, no. 38, pp. 18344–18356, 2018

[58] K. H. Kim, D. J. Lee, K. M. Cho, S. J. Kim, J.-K. Park, and H.-T. Jung, 'Complete magnesiothermic reduction reaction of vertically aligned mesoporous silica channels to form pure silicon nanoparticles', *Sci Rep*, vol. 5, no. 1, p. 9014, Aug. 2015

[59] Y. Tan, T. Jiang, and G. Z. Chen, 'Mechanisms and Product Options of Magnesiothermic Reduction of Silica to Silicon for Lithium-Ion Battery Applications', *Front. Energy Res.*, vol. 9, 2021

[60] M. Ashuri, Q. He, K. Zhang, S. Emani, and L. L. Shaw, 'Synthesis of hollow silicon nanospheres encapsulated with a carbon shell through sol–gel coating of polystyrene nanoparticles', *J Sol-Gel Sci Technol*, vol. 82, no. 1, pp. 201–213, Apr. 2017

[61] J. Entwistle and S. Patwardhan, 'The Application of Magnesiothermic Reduction of Silica to Produce Porous Silicon for Lithium Ion Batteries', *Meet. Abstr.*, vol. MA2019-01, no. 2, p. 295, May 2019

[62] F. Holtstiege, A. Wilken, M. Winter, and T. Placke, 'Running out of lithium? A route to differentiate between capacity losses and active lithium losses in lithium-ion batteries', *Phys. Chem. Chem. Phys.*, vol. 19, no. 38, pp. 25905–25918, Oct. 2017

[63] H. Park, M. Kim, F. Xu, C. Jung, S. M. Hong, and C. M. Koo, 'In situ synchrotron wide-angle X-ray scattering study on rapid lithiation of graphite anode via direct contact method for Li-ion capacitors', *Journal of Power Sources*, vol. 283, pp. 68–73, Jun. 2015

[64] F. Holtstiege, A. Wilken, M. Winter, and T. Placke, 'Running out of lithium? A route to differentiate between capacity losses and active lithium losses in lithium-ion batteries', *Phys. Chem. Chem. Phys.*, vol. 19, no. 38, pp. 25905–25918, Oct. 2017

[66] H. J. Kim *et al.*, 'Controlled Prelithiation of Silicon Monoxide for High Performance Lithium-Ion Rechargeable Full Cells', *ACS Publications*, Dec. 24, 2015

[67] Q. Meng, G. Li, J. Yue, Q. Xu, Y.-X. Yin, and Y.-G. Guo, 'High-Performance Lithiated SiOX Anode Obtained by a Controllable and Efficient Prelithiation Strategy', *ACS Applied Materials & Interfaces*, vol. 11, Aug. 2019

[68] J. Entwistle, A. Rennie, and S. Patwardhan, 'A review of magnesiothermic reduction of silica to porous silicon for lithium-ion battery applications and beyond', *J. Mater. Chem. A*, vol. 6, no. 38, pp. 18344–18356, 2018

[69] C. T. Kresge, M. E. Leonowicz, W. J. Roth, J. C. Vartuli, and J. S. Beck, 'Ordered mesoporous molecular sieves synthesised by a liquid-crystal template mechanism', *Nature*, vol. 359, no. 6397, pp. 710–712, Oct. 1992

[70] D. Zhao, 'Triblock Copolymer Syntheses of Mesoporous Silica with Periodic 50 to 300 Angstrom Pores', *Science*, vol. 279, no. 5350, pp. 548–552, Jan. 1998

[71] J. Florek, R. Guillet-Nicolas, and F. Kleitz, Eds., '4. Ordered mesoporous silica: synthesis and applications', in *Functional Materials*, De Gruyter, 2014, pp. 61–100.

[72] J. N. Israelachvili, D. J. Mitchell, and B. W. Ninham, 'Theory of self-assembly of hydrocarbon amphiphiles into micelles and bilayers', *J. Chem. Soc., Faraday Trans. 2*, vol. 72, p. 1525, 1976

[73] Y. S. Lee, *Self-Assembly and Nanotechnology*. Hoboken, NJ, USA: John Wiley & Sons, Inc., p.60-61, 2008

[74] Q. Huo, D. I. Margolese, and G. D. Stucky, 'Surfactant Control of Phases in the Synthesis of Mesoporous Silica-Based Materials', *Chem. Mater.*, vol. 8, no. 5, pp. 1147–1160, Jan. 1996

[75] Y. Han and D. Zhang, 'Ordered mesoporous silica materials with complicated structures', *Current Opinion in Chemical Engineering*, vol. 1, no. 2, pp. 129–137, May 2012

[76] Y. Sun *et al.*, 'Formation pathways of mesoporous silica nanoparticles with dodecagonal tiling', *Nat Commun*, vol. 8, no. 1, p. 252, Dec. 2017

[77] D. Zhao, Q. Huo, J. Feng, B. F. Chmelka, and G. D. Stucky, 'Nonionic Triblock and Star Diblock Copolymer and Oligomeric Surfactant Syntheses of Highly Ordered, Hydrothermally Stable, Mesoporous Silica Structures', *J. Am. Chem. Soc.*, vol. 120, no. 24, pp. 6024–6036, Jun. 1998

[78] J. Fan *et al.*, 'Cubic Mesoporous Silica with Large Controllable Entrance Sizes and Advanced Adsorption Properties', *Angew. Chem. Int. Ed.*, vol. 42, no. 27, pp. 3146–3150, Jul. 2003

[79] C. T. Kresge, M. E. Leonowicz, W. J. Roth, J. C. Vartuli, and J. S. Beck, 'Ordered mesoporous molecular sieves synthesised by a liquid-crystal template mechanism', *Nature*, vol. 359, no. 6397, pp. 710–712, Oct. 1992

[80] D. Zhao, Q. Huo, J. Feng, B. F. Chmelka, and G. D. Stucky, 'Nonionic Triblock and Star Diblock Copolymer and Oligomeric Surfactant Syntheses of Highly Ordered, Hydrothermally Stable, Mesoporous Silica Structures', *J. Am. Chem. Soc.*, vol. 120, no. 24, pp. 6024–6036, Jun. 1998

[81] A. Carlsson, M. Kaneda, Y. Sakamoto, O. Terasaki, R. Ryoo, and S. H. Joo, 'The structure of MCM-48 determined by electron crystallography', *Journal of Electron Microscopy*, vol. 48, no. 6, pp. 795–798, Jan. 1999

[82] T.-W. Kim, F. Kleitz, B. Paul, and R. Ryoo, 'MCM-48-like Large Mesoporous Silicas with Tailored Pore Structure: Facile Synthesis Domain in a Ternary Triblock Copolymer−Butanol−Water System', *J. Am. Chem. Soc.*, vol. 127, no. 20, pp. 7601–7610, May 2005

[83] X. Du and S. Z. Qiao, 'Dendritic Silica Particles with Center-Radial Pore Channels: Promising Platforms for Catalysis and Biomedical Applications', *Small*, vol. 11, no. 4, pp. 392–413, 2015

[84] Y. Lai, J. R. Thompson, and M. Dasog, 'Metallothermic Reduction of Silica Nanoparticles to Porous Silicon for Drug Delivery Using New and Existing Reductants', *Chem. Eur. J.*, vol. 24, no. 31, pp. 7913–7920, Jun. 2018

[85] J. Entwistle, A. Rennie, and S. Patwardhan, 'A review of magnesiothermic reduction of silica to porous silicon for lithium-ion battery applications and beyond', *J. Mater. Chem. A*, vol. 6, no. 38, pp. 18344–18356, 2018

[86] B. G. Gribov and K. V. Zinov'ev, 'Preparation of High-Purity Silicon for SOlar Cells', *Inorganic Materials*, vol. 39, no. 7, pp. 653–662, 2003

[87] L. Batchelor, A. Loni, L. T. Canham, M. Hasan, and J. L. Coffer, 'Manufacture of Mesoporous Silicon from Living Plants and Agricultural Waste: An Environmentally Friendly and Scalable Process', *Silicon*, vol. 4, no. 4, pp. 259–266

[88] K. H. Kim, D. J. Lee, K. M. Cho, S. J. Kim, J.-K. Park, and H.-T. Jung, 'Complete magnesiothermic reduction reaction of vertically aligned mesoporous silica channels to form pure silicon nanoparticles', *Sci Rep*, vol. 5, no. 1, p. 9014, Aug. 2015

[89] I. S. Curtis, R. J. Wills, M. Dasog, 'Photocatalytic hydrogen generation using mesoporous silicon nanoparticles: influence of magnesiothermic reduction conditions and nanoparticle aging on the catalytic activity', Nanoscale, 2021, 13, 2685.

[90] M. Barati, S. Sarder, A. McLean, and R. Roy, 'Recovery of silicon from silica fume', *Journal of Non-Crystalline Solids*, vol. 357, no. 1, pp. 18–23, Jan. 2011

[91] N. Liu, K. Huo, M. T. McDowell, J. Zhao, and Y. Cui, 'Rice husks as a sustainable source of nanostructured silicon for high performance Li-ion battery anodes', *Sci Rep*, vol. 3, no. 1, p. 1919

[92] L. Shi, W. Wang, A. Wang, K. Yuan, and Y. Yang, 'Understanding the impact mechanism of the thermal effect on the porous silicon anode material preparation via magnesiothermic reduction', *Journal of Alloys and Compounds*, vol. 661, pp. 27–37

[93] H. Jia, P. Gao, J. Yang, J. Wang, Y. Nuli, and Z. Yang, 'Novel Three-Dimensional Mesoporous Silicon for High Power Lithium-Ion Battery Anode Material', *Adv. Energy Mater.*, vol. 1, no. 6, pp. 1036–1039, Nov. 2011

[94] H.-C. Tao, L.-Z. Fan, and X. Qu, 'Facile synthesis of ordered porous Si@C nanorods as anode materials for Li-ion batteries', *Electrochimica Acta*, vol. 71, pp. 194–200, Jun. 2012

[95] L. Pan, H. Wang, D. Gao, S. Chen, L. Tan, and L. Li, 'Facile synthesis of yolk–shell structured Si–C nanocomposites as anodes for lithium-ion batteries', *Chem. Commun.*, vol. 50, no. 44, pp. 5878–5880, May 2014

[96] M. Ashuri, Q. He, and L. L. Shaw, 'Silicon as a potential anode material for Li-ion batteries: where size, geometry and structure matter', *Nanoscale*, vol. 8, no. 1, pp. 74–103, Dec. 2015

[97] J. A. Dean and N. A. Lange, Eds., *Lange's handbook of chemistry*, 15. ed. New York, +NY: McGraw-Hill, 1999, p.6.101

[98] X. Liu, C. Giordano, and M. Antonietti, 'A molten-salt route for synthesis of Si and Ge nanoparticles: chemical reduction of oxides by electrons solvated in salt melt', *J. Mater. Chem.*, vol. 22, no. 12, p. 5454, 2012

[99] W. Luo *et al.*., 'Efficient Fabrication of Nanoporous Si and Si/Ge Enabled by a Heat Scavenger in Magnesiothermic Reactions', *Sci Rep*, vol. 3, no. 1, p. 2222, Dec. 2013

[100] L. Batchelor, A. Loni, L. T. Canham, M. Hasan, and J. L. Coffer, 'Manufacture of Mesoporous Silicon from Living Plants and Agricultural Waste: An Environmentally Friendly and Scalable Process', *Silicon*, vol. 4, no. 4, pp. 259–266

[101] E. Juère, R. Caillard, D. Marko, G. Del Favero, and F. Kleitz, 'Smart Protein-Based Formulation of Dendritic Mesoporous Silica Nanoparticles: Toward Oral Delivery of Insulin', *Chem. Eur. J.*, vol. 26, no. 23, pp. 5195–5199, Apr. 2020

[102] T.-W. Kim, F. Kleitz, B. Paul, and R. Ryoo, 'MCM-48-like Large Mesoporous Silicas with Tailored Pore Structure: Facile Synthesis Domain in a Ternary Triblock Copolymer−Butanol−Water System', *J. Am. Chem. Soc.*, vol. 127, no. 20, pp. 7601–7610, May 2005

[103] F. Kleitz, S. Hei Choi, and R. Ryoo, 'Cubic Ia3d large mesoporous silica: synthesis and replication to platinum nanowires, carbon nanorods and carbon nanotubes, *Chem. Commun.*, no. 17, p. 2136, 2003

[104] M. Leclerc and R. Gauvin, Eds., *Functional materials: for energy, sustainable development and biomedical sciences*. Berlin: De Gruyter, 2014.

[105] W. Luo *et al.*., 'Efficient Fabrication of Nanoporous Si and Si/Ge Enabled by a Heat Scavenger in Magnesiothermic Reactions', *Sci Rep*, vol. 3, no. 1, p. 2222, Dec. 2013

[106] F. Kleitz, S. Hei Choi, and R. Ryoo, 'Cubic Ia3d large mesoporous silica: synthesis and replication to platinum nanowires, carbon nanorods and carbon nanotubes', Chem. Commun., no. 17, p. 2136, 2003

[107] J. Hochstrasser *et al.,* 'Morphology–transport relationships for SBA-15 and KIT-6 ordered mesoporous silicas', Phys. Chem. Chem. Phys., vol. 22, no. 20, pp. 11314–11326, 2020

[108] J. Hochstrasser *et al.,* 'Morphology–transport relationships for SBA-15 and KIT-6 ordered mesoporous silicas', Phys. Chem. Chem. Phys., vol. 22, no. 20, pp. 11314–11326, 2020

[109] T.-W. Kim, P.-W. Chung, and V. S.-Y. Lin, 'Facile Synthesis of Monodisperse Spherical MCM-48 Mesoporous Silica Nanoparticles with Controlled Particle Size', Chem. Mater., vol. 22, no. 17, pp. 5093–5104, Sep. 2010

[110] E. Juère, R. Caillard, D. Marko, G. Del Favero, and F. Kleitz, 'Smart Protein-Based Formulation of Dendritic Mesoporous Silica Nanoparticles: Toward Oral Delivery of Insulin', Chem. Eur. J., vol. 26, no. 23, pp. 5195–5199, Apr. 2020

[111] X. Liu, C. Giordano, and M. Antonietti, 'A molten-salt route for synthesis of Si and Ge nanoparticles: chemical reduction of oxides by electrons solvated in salt melt', *J. Mater. Chem.*, vol. 22, no. 12, p. 5454, 2012

[112] J. Betz, L. Nowak, M. Winter, T. Placke, and R. Schmuch, 'An Approach for Pre-Lithiation of Li1+xNi0.5Mn1.5O4 Cathodes Mitigating Active Lithium Loss', *J. Electrochem. Soc.*, vol. 166, no. 15, p. A3531, Oct. 2019

[113] M. G. Scott, A. H. Whitehead, and J. R. Owen, 'Chemical Formation of a Solid Electrolyte Interface on the Carbon Electrode of a Li-Ion Cell', *J. Electrochem. Soc.*, vol. 145, no. 5, pp. 1506–1510, May 1998

[114] X. Li *et al.*, 'Mesoporous silicon sponge as an anti-pulverization structure for high-performance lithium-ion battery anodes', *Nature Communications*, vol. 5, no. 1, Art. no. 1, Jul. 2014

[115] F. Kleitz, S. H. Choi, and R. Ryoo, 'Cubic Ia3d large mesoporous silica: synthesis and replication to platinum nanowires, carbon nanorods and carbon nanotubes', *Chem. Commun.*, no. 17, pp. 2136–2137, Aug. 2003

[116] J. Hochstrasser *et al.*, 'Morphology–transport relationships for SBA-15 and KIT-6 ordered mesoporous silicas', *Phys. Chem. Chem. Phys.*, vol. 22, no. 20, pp. 11314–11326, 2020

[117] T.-W. Kim, P.-W. Chung, and V. S.-Y. Lin, 'Facile Synthesis of Monodisperse Spherical MCM-48 Mesoporous Silica Nanoparticles with Controlled Particle Size', *Chem. Mater.*, vol. 22, no. 17, pp. 5093–5104, Sep. 2010

[118] E. Juère, R. Caillard, D. Marko, G. Del Favero, and F. Kleitz, 'Smart Protein-Based Formulation of Dendritic Mesoporous Silica Nanoparticles: Toward Oral Delivery of Insulin', *Chemistry – A European Journal*, vol. 26, no. 23, pp. 5195–5199, Apr. 2020

[119] F. Kleitz, S. H. Choi, and R. Ryoo, 'Cubic Ia3d large mesoporous silica: synthesis and replication to platinum nanowires, carbon nanorods and carbon nanotubes', *Chem. Commun.*, no. 17, pp. 2136–2137

[120] T.-W. Kim, P.-W. Chung, and V. S.-Y. Lin, 'Facile Synthesis of Monodisperse Spherical MCM-48 Mesoporous Silica Nanoparticles with Controlled Particle Size', *Chem. Mater.*, vol. 22, no. 17, pp. 5093–5104

[121] T.-W. Kim, P.-W. Chung, and V. S.-Y. Lin, 'Facile Synthesis of Monodisperse Spherical MCM-48 Mesoporous Silica Nanoparticles with Controlled Particle Size', *Chem. Mater.*, vol. 22, no. 17, pp. 5093–5104

[122] M. Thommes *et al.*, 'Physisorption of gases, with special reference to the evaluation of surface area and pore size distribution (IUPAC Technical Report)', *Pure and Applied Chemistry*, vol. 87, no. 9–10, pp. 1051–1069, Oct. 2015

[123] I. W. Sutapa, A. W. Wahab, P. Taba, and N. L. Nafie, 'Synthesis and Structural Profile Analysis of the MgO Nanoparticles Produced Through the Sol-Gel Method Followed by Annealing Process', *Oriental Journal of Chemistry*, vol. 34, no. 2, pp. 1016–1025

[124] W. Luo *et al.*, 'Efficient Fabrication of Nanoporous Si and Si/Ge Enabled by a Heat Scavenger in Magnesiothermic Reactions', *Sci Rep*, vol. 3, no. 1, p. 2222, Dec. 2013

[125] K. K. Larbi, M. Barati, and A. McLean, 'Reduction behaviour of rice husk ash for preparation of high purity silicon', *Canadian Metallurgical Quarterly*, vol. 50, no. 4, pp. 341–349, Oct. 2011

[126] Y. Zhang and J. Huang, 'Hierarchical nanofibrous silicon as replica of natural cellulose substance', *J. Mater. Chem.*, vol. 21, no. 20, p. 7161, 2011

[127] K. K. Larbi, M. Barati, and A. McLean, 'Reduction behaviour of rice husk ash for preparation of high purity silicon', *Canadian Metallurgical Quarterly*, vol. 50, no. 4, pp. 341–349, Oct. 2011

[128] Y. Zhang and J. Huang, 'Hierarchical nanofibrous silicon as replica of natural cellulose substance', *J. Mater. Chem.*, vol. 21, no. 20, p. 7161, 2011

[129] E. Radvanyi *et al.*, 'Study of lithiation mechanisms in silicon electrodes by Auger Electron Spectroscopy', *J. Mater. Chem. A*, vol. 1, no. 16, pp. 4956–4965

[130] L. Li, J. Sui, and W. Qin, 'Synthesis of high purity Li2CO3 and MgCO3·3H2O in a homogeneous-like organic phase', *Chinese Journal of Chemical Engineering*, vol. 27, no. 5, pp. 1230–1234